Chapter 7
Detectors for Electron and X-ray Scattering and Imaging Experiments

Alexander Ziegler and Heinz Graafsma

Abstract Suitable detectors for these expensive and highly complex experimental instruments described in the previous chapters are a key factor to consider, primarily because if one cannot visualize or record the experimental results with an appropriate detector, any experiment will fail. The general challenge for all position-, energy-, and time-resolving detector systems is the fulfillment of stringent requirements for direct X-ray and electron detection experiments. These include a priori a high detection sensitivity and efficiency, but most important is coping with extremely high flux (10^{12} highly energetic X-ray photons or 10^{8} 300 kV electrons per second), exhibiting appropriate radiation hardness to maintain proper detection sensitivity and operability, low electronic noise for finest energy resolution in single-photon counting mode, and high frame rates for high time resolution. Parameters such as the Modulation Transfer Function (MTF), the Detector Quantum Efficiency (DQE), the dynamic range, pixel size, sensitivity, linearity, uniformity, background noise, read out speed, and reliability (or life time) among other characteristics will need to be considered to decide which detector design is best for what application. There are a variety of designs in the development and/or prototype stage. Costs are high, because most are produced using expensive wafer fabrication processes. A point of consideration is flexibility, adaptability, and how

---

A. Ziegler (✉)
Microscopy and Microanalysis Unit, The University of the Witwatersrand,
1 Jan Smuts Ave., Johannesburg 2000, South Africa
e-mail: alexander.ziegler@wits.ac.za

H. Graafsma
Photon-Science Detector Group,
Deutches Elektronen-Synchrotron, DESY, Notkestr. 85, D-22607 Hamburg, Germany
e-mail: heinz.graafsma@desy.de

H. Graafsma
STC Research Center, University of Mid-Sweden, 85107 Sundsvall, Sweden

A. Ziegler et al. (eds.), *In-situ Materials Characterization*,
Springer Series in Materials Science 193, DOI: 10.1007/978-3-642-45152-2_7,

swift detector parameters can be changed. The trend at high-end, multi-national, multi-user scientific research facilities (Synchrotrons, FELs) however, is to operate dedicated, non-transferable detectors for specialized applications, whereas the medium to small scale research facilities may well decide for a more versatile, multi-purpose detector. The following sections will address detectors for electrons and detectors for X-ray photons separately. Development efforts for these detector types overlap, in part due to the high costs involved, and in part due to the compatibility of some developmental stages and components for both detector types.

7.1 Detectors for Electrons

7.1.1 Introduction

Detectors for electron imaging have continuously been evolving over the past three decades. Before the 1980s photographic film was the only choice for suitable electron image recording. The transition from the very traditional photographic film over imaging plates, indirect detection techniques, to the novel direct detection techniques has provided electron microscopists with a number of options for image recording. In brief, the traditional photographic film comes with the associated light sensitive negatives, their development in the dark room and printing on photographic paper. The imaging plates use less light sensitive negatives, but still require digitization and printing. The indirect detection technique using Charge Coupled Devices (CCD) require electron-to-light conversion methods—i.e., scintillators and CCDs that operate in the visible range of the spectrum. Finally, the novel digital detectors use direct conversion of the incoming particle, electron or photon, to an electrical signal and perform digitization in the detector front-end.

The motivation for the transition from the classical photographic film over imaging plates to electronic, CCD-based, indirect electron detectors is the sheer advantage of having a digital image, which is directly and immediately viewable and adjustable on a computer screen at the time of recording. This is certainly more user friendly than having to deal with negatives and their developing conditions (and the capabilities of the microscopist), and the post-microscope session scanning of negatives or image plates. The biggest disadvantage of photographic film or the imaging plate, is that mishaps and system failures can often only be seen after the negatives have been developed or the imaging plate read out. The possibilities that digital imaging offer—not only in terms of direct image acquisition, but also for any ensuing on-line and/or live image processing—have opened doors to a number of research fields, in particular but not exclusively, in-situ microscopy, electron tomography, and remote microscopy (where the operator may be located in an adjacent office or even in a different city or country). Digital detectors have therefore become the de-facto standard in electron optical imaging.

However, none of the electron imaging devices is perfect. From the plain image recording perspective each device has advantages and disadvantages that need to be taken into account depending on the application.

7.1.2 Electron Image Recording Devices

7.1.2.1 Photographic Film

Electron microscopy conform photographic film consists of an emulsion of fine silver halide particles (3–6 μm in size) suspended (1:1) in an approximately 20 μm thick layer of gelatine. The film thickness corresponds approximately to the mean free path of 120 kV electrons—purposefully designed so that these electrons scatter statistically only once while traversing the film. Multiple scattering inside the film layer would only degrade the quality and the resolution of the recorded image, because lateral scattering and propagation of the primary electron away from the incident direction would only generate metallic silver particles where no incident electron may have hit the film. The silver halide grains convert to metallic silver grains when exposed to the electron beam. The energy required for this conversion is approximately 7 eV, clearly indicating that one single high-energy electron in an electron microscope can easily generate 10^4 silver atoms—representing a large portion of one single silver halide grain in the film emulsion. This process stores a latent image in the film made of silver halide grains. In comparison, film exposure to visible light of about 3 eV requires a collective process involving many photons to convert the silver halide atoms to metallic silver atoms. During chemical development of the photographic film in the dark room, the silver grains containing the latent electron image information are fully converted to metallic silver, whereas the non-irradiated and therefore non-converted silver halide grains are removed.

For photographic film, its non-linearity, the limited possibilities to reduce the inherent noise characteristics, and the limited dose (or intensity) range, plus the strong dependence on the film developing conditions, make film not quite suitable for applications like low-dose imaging, or where electron intensity quantification is important. One has for decades recorded electron diffraction patterns on film, and it has shown very suitable for the recording of high-intensity peaks (except for the central diffraction peak). However, with the non-linear characteristics of film, and its best operating conditions in an intermediate yet limited dose (intensity) range, film tends to reduce the true intensity of the very high-intensity peaks, appropriately represent the medium-intensity peaks, and obscure the low-intensity peaks below recognition. Precise quantification of the electron intensities however, is important for convergent beam electron diffraction patterns. With film, this is done by measuring the optical density in a film scanner. The optical density here is defined as the fraction of light that is transmitted by the film. However, considering the non-linearity of film the quantification allows reconstructing the true intensities only when knowing the non-linear relation between optical density and dose. Systematic errors affect the results significantly. Nevertheless, in some cases experimental and theoretical intensities can be matched with an accuracy of close to 99 %.

7.1.2.2 Imaging Plate

An imaging plate consist of an approximately 110 μm thick photo-stimulable layer of phosphor grains (BaFX $\{X = \mathrm{Cl}, \mathrm{Br}\}$, doped with Eu^{2+}) that is encapsulated by a flat sheet of plastic support below and a protective layer above. The grains are nominally regarded as pixels 25×25 μm in size. This flexible sheet can be used just like film in the standard film cassette of the microscope. During recording, the phosphor layer stores the electron energy in the potential well of the defect states of the phosphor grains. In essence, by ionizing Eu^{2+} to Eu^{3+}, some of the electrons are excited to the conduction band and are trapped in F^{+}-centers of the crystal creating a metastable state. This process allows the phosphor grains to store a latent image. However, at room temperature these defect states do have a limited life time of up to a few days, during which one can digitally read out the imaging plates many times. However, each read out reduces the amount of energy stored, and as such the signal decreases as the number of read outs increases. The read out mechanisms relies on the narrow spectral range of a He–Ne laser that scans the imaging plate causing luminescent light emission from the imaging plate that is captured, logarithmically amplified by a photomultiplier, and digitized into 14 bits. Exposing the imaging plate to white light erases the latent image by irradiating the phosphor with sufficient photon energy, causing the removal of the defect states in the phosphor grains and a back-conversion of the Eu^{3+} ions to Eu^{2+}, such that the imaging plate can be re-used. All imaging characteristics are the combined response of the imaging plate and the read out device. One cannot isolate the characteristics of the imaging plate from the reader.

Imaging plates exhibit a highly linear counts versus electron dose behavior, offer possibilities to reduce the inherent noise characteristics by adjusting the read out device to a high sensitivity setting, and their broad dose (or intensity) range in which they operate, make imaging plates very suitable for low-dose and high-resolution imaging applications. They are not very good at recording and storing high electron doses (intensities) as the inherent noise characteristics increase dramatically with dose. This signal-to-noise limitation is due to granular variations of the phosphor. The 25×25 μm pixel of an image plate consist of a varying number of Eu^{2+} doped phosphor grains (due to grain size variations). Consequently, the number of Eu atoms varies from pixel to pixel, and concomitantly the gain factor, which in return causes large variations in gain across the image plate, contributing to the intensity dependent noise, also known as granular noise. In principle—and this is technically feasible—the read out device would need to be precisely aligned with the image plate inserted, such that it normalizes these gain variations. For this to work out properly, the positioning and alignment error of the image plate would need to be less than 1 μm for every read out. Another remedy to reduce the gain variations among pixels is to reduce the grain size of the phosphor, such that a more homogeneous distribution of grains (and Eu atoms) can be achieved. Binning of pixels is another method that allows reducing gain variations, however at the expense of spatial resolution.

7.1.2.3 CCD-Based Indirect Electron Detector

The working principle of the CCD-based, indirect detection strategy involves three processes, namely (1) capturing and converting electrons to photons via a phosphor scintillator, (2) guiding these photons to a light sensitive CCD array via fiber optical coupling, and (3) converting the photons back into an electronic signal via electron-hole pair generation in the CCD pixel, which can be read out consecutively to form an image.

This indirect electron detection approach is characterized by a number of optical interfaces within the entire detector assembly, resulting in multiple scattering events and a subsequent loss in resolution. The scintillator layer at the very top of the detector assembly consists of a material that converts electrons to photons. A variety of powder phosphors, in particular Gadolinium Oxysulphide (GOS) phosphor, as well as an Yttrium Aluminum Garnet (YAG) single crystal doped with Cerium serve this purpose. Both materials have significantly different photon yields. The generation of photons in GOS phosphor is about twice as high as in YAG, resulting in a highly sensitive detector if equipped with GOS phosphor. Yet, the variations in GOS powder morphology, especially grain size, cause a larger variance in response characteristics. In contrast, the YAG crystal exhibits a more uniform photon emission and is more resistant to electron beam irradiation—hence a favorite material for CCD based electron detector manufacturers. Additionally, scintillator thickness affects electron-to-photon conversion—the gain. A thicker layer emits more photons than a thinner scintillator, allowing the tailoring of detector sensitivity according to the application. Generally, low-dose applications call for the enhanced gain found in thicker scintillators, because the sample consists of beam sensitive, low-contrast matter (biological samples), and a decent signal-to-noise ratio is critical. Instead, a thin scintillator is used for high-dose applications, examining more beam resistant samples that exhibit better contrast, and aiming at high spatial resolution in the image.

While thicker scintillators yield higher gain, the result is not independent of the variable accelerating voltage of the electrons in electron microscopes (in most cases anywhere between 30 and 300 kV). Lower accelerating voltages and thus slower incident electrons have a shorter mean free path—that is the distance between consecutive scattering events—than higher accelerating voltages (and faster electrons). Consequently, a slow electron will scatter more often in a given scintillator thickness, yielding a higher gain than a fast electron. This is shown in Fig. 7.1 where the dependence of gain on accelerating voltage is plotted for a CCD-based electron detector in comparison to an imaging plate.

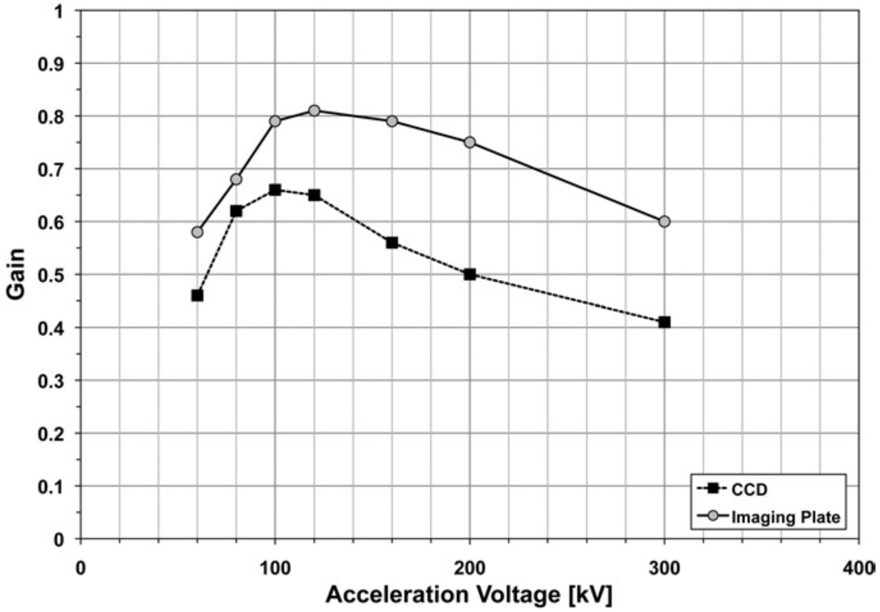

Fig. 7.1 The dependence of detector gain on accelerating voltage—comparing a CCD-based electron detector to an imaging plate

The CCD-based detector is equipped with a fiber-coupled YAG scintillator, whereas the imaging plate pixels consist of phosphor powder. Observe how the gain peaks at 100–120 kV accelerating voltage and drops off at higher accelerating voltages. The scintillator thickness of this particular detector shown, as well as the imaging plate was designed to yield highest gain for 100–120 kV mircoscopes/applications. (Note: 100–120 kV or even 60 kV applications are not to be confused with low-dose applications. Low-dose microscopy can also be performed at 300 kV. Low-dose only stands for low-intensity, not low-accelerating voltages.)

As mentioned before, it can also be observed that the YAG crystal is less gain efficient than the phosphor used in the imaging plate.

Electron scattering occurs in all scintillators, resulting in photon generation across a number of phosphor grains, or alternatively, across a number of optical fibers that guide the photons to the CCD pixel array. Fiber-coupling connects each pixel via an optical fiber with the scintillator. Thus, one single electron that ideally should activate only one corresponding pixel on the CCD may in reality—due to scattering—activate some neighboring pixels too. While a thicker scintillator may generate a larger number of photons, it also exhibits a larger spatial spreading of these photons over a larger number of optical fibers. Thus spatial resolution in the recorded image is compromised. Additionally to the spreading of photons, reflection of photons back into the YAG scintillator (from both, the entry and exit plane) contributes to lateral signal spreading and image blur. Photons that enter the optical fibers at high incident angles can—provided the internal reflection conditions are such that the acceptance cone (critical angle) is not too small—cause a leaking of photons out of fibers adding to the image blur and loss of spatial resolution.

An alternative to fiber-coupling the scintillator with the CCD pixel array is lens-coupling. Lens-coupling allows for a somewhat higher flexibility in detector assembly and design, but it is less efficient than fiber-coupling. Fiber-coupling is done by permanently attaching a set of parallel fibers (bound together forming a block of fibers) to the scintillator and an identical block of fibers to the CCD. When assembling the detector, the fiber blocks from the scintillator and the CCD need to be aligned properly and connected optically. This is best done via a thin film of oil spread between the blocks of optical fibers. In any case, the measured overall response of the detector is a combined response of scintillator, fiber optics, CCD array, and the interfaces therein.

Compromised spatial resolution due to electron scattering and the ensuing photon propagation in the optical fibers is the major limiting factor for the CCD based electron detectors. Although the individual pixel in the CCD array is small (the majority of CCD have 14 or 24 μm pixels), this is rarely the actual image resolution as usually more than one pixel is activated by one single incident electron.

Very high electron intensities, encountered for example in the central spot of a diffraction pattern, over saturates the CCD—even if blocked with the beam stop of the electron microscope, the brightness “spills over”, causing oversaturation of an entire array of CCD pixel rows and columns. There are some CCD based detectors that can handle higher intensities, with the consequence that they do not perform well in the medium to low electron intensity regime.

Beside the image quality compromising effects in the scintillator and fiber optics, the CCD based electron detectors are also characterized by significant levels of conversion, readout and dark-current noise in the pixel array. The dark current and the readout noise (from here on denoted as background noise) are proportional to the temperature of the pixel array and the thermally excited electrons inside each pixel are proportional to the exposure time. Experimentally they are hard to distinguish. This background noise can be reduced by cooling the detector down to −25 °C—usually with Peltier cooling elements. Both, the readout and the dark current noise are independent of illumination, dominating in low-dose images, whereas the photon-to-electron conversion noise in the pixel increases with increasing illumination. The latter type of noise can strongly affect the signal-to-noise ratio at high-dose applications. However, it can be minimized by performing a gain normalization of the entire detector area prior to image recording. To understand this, consider each pixel as an independent detector. Hence, the CCD array consists of many small, separate detectors, each one with its own set of background and conversion noise. The conversion noise in each of them results in a distinctive gain response that increases proportional to the illumination intensity, and each individual gain response varies constantly during continuous exposure. By recording a number of full sized (entire detector array) images under uniform illumination, these gain variations can be averaged and normalized to adjust the pixel-to-pixel variations across the entire pixel array. Similarly, one can perform a dark current assessment by recording a number of dark current images (no illumination), which for obvious reasons include the readout noise. Both, the resulting gain normalization and the dark current images are subtracted from each image that is recorded during the ensuing microscope session. In contrast, this type of digital image processing for noise reduction purposes cannot be performed with photographic film or the imaging plate.

The CCD-based indirect electron detectors exhibit a highly linear counts versus electron dose behavior, and their broad dose (or intensity) range (also called dynamic range) in which they operate, make these digital detectors very suitable for medium- to high-dose applications. However, considering the disadvantages of the indirect electron detection strategy, especially the inferior spatial resolution due to relatively large pixels, and the lack of sensitivity in the low-dose domain due to the high levels of inherent background noise, are motivation enough to continue with electron detector development.

Thus, the reason and motivation to further transition from the indirect to the next level—direct electron detection techniques—is the prospect to finally operate an electron detector with all the digital and user friendly advantages of the existing CCD based detector systems, yet with better characteristics. In particular, the ability to investigate highly beam sensitive samples, especially in the soft-matter and the life sciences is sufficient motivation to advocate further detector development. The direct electron detection technique has the potential to provide a much more sensitive imaging device, because its noise and spatial resolution figures can be up to 10 times better. Single electron detection is the goal here. These enhanced capabilities of direct electron detectors have inimitable consequences, because it allows taking on the major problem in beam sensitive investigations using electrons: radiation damage. Radiation damage to the sample is also found in experiments using other high-brightness radiation sources, i.e., synchrotron and X-ray Free Electron Lasers (XFEL). Fact is that the ultimate resolution of structural studies using electrons and/or X-rays is limited by the radiation sensitivity of the sample.

There are in principle two approaches to overcome the degrading effects of radiation damage. One is to perform single-shot experiments, where a large number of electrons ($>10^8$) or X-ray photons ($>10^{12}$) is directed in one single, but very short pulse (10–1000 fs) onto the specimen. The idea here is to record the image (or spectral information) faster than the damage mechanism can unfold and destroy the sample. Generally, the damage mechanisms can be associated with the ionization of atoms due to the incoming X-rays. Once ionized and exhibiting a charge, the subsequent effect of so many same-charge ions, which are still densely packed in their original volume causes a so-called Coulomb explosion. Such ultrafast experiments can be performed and they are currently of high scientific interest (see Chaps. 2 and 4), concomitant with the development of XFELs. The second approach pertains so far only to the use of electrons and entails performing single-electron experiments allowing for energy and heat dissipation within the sample and thus avoiding thermal damage mechanisms to destroy the sample. Both approaches have in common that they require highly sensitive direct detectors. Additionally, the very large dynamic range of these novel detectors becomes very important here.

In order to be able to objectively compare electron imaging devices one needs to understand the critical parameters that are generally used to characterize detectors. The concepts of spatial resolution (pixel size) and the Modulation Transfer Function (MTF), noise and the Detector Quantum Efficiency (DQE), dynamic range, linearity, and uniformity are the parameters of interest. While we will discuss all of them in the following section, the MTF, the DQE, and the dynamic range, are the primary parameters used to compare electron detector types here. There is an increasing demand and an enormous list of publications (too many to list them all here) that all aim at uniform and standardized detector characterization methods. However, due to the large variability of detector designs and applications, this task is not as easy and straightforward as it may seem [1]. The medical imaging community has their standards, for instance the IEC-62220-1 for the determination of the DQE. Applying this standard to similar yet different detectors in other disciplines proves practically impossible in many cases.

7.1.3 Critical Parameters for Detector Characterization

7.1.3.1 Modulation Transfer Function

The MTF measures the ability of a detector to distinguish a black-white transition. Ideally, a black-and-white variable-width line pattern (Fig. 7.2) would need to be placed right in front of the detector and an image recorded, and even more ideally in both the horizontal and the vertical direction. The ability of any image recording device to perfectly record and display such black-white features will decrease (and thus the MTF decline) as the features—here the line spacing—become smaller and smaller. Eventually, the black-white-black will turn into shades of grey and the ability to discern accordingly small features in a high-resolution image will vanish.

However, such an ideal fine line pattern cannot be fabricated with line spacings small enough (<1 nm) to cover the entire detector's ability to transfer spatial frequencies. As one alternative to such a fine line pattern only one black-white transition—a sharp knife-edge—is used to record images for the MTF analysis. A second alternative is the noise approach. In the latter a series of noise images are recorded and analyzed to extract the required information for the MTF.

In essence, the MTF measures how contrast is transmitted within the detector. Contrast is defined as

$$Contrast = \frac{I_{\max} - I_{\min}}{I_{\max} + I_{\min}} \tag{7.1}$$

where $I_{\max}$ and $I_{\min}$ are the intensity maxima and minima respectively. Figure 7.3 shows a simulation of the effect the MTF has on a set of parallel lines that vary in separation (increasing distance from 1 to 11). The top row (a) depicts the ideal image without blurring of the signal (perfect contrast, perfect MTF = ideal

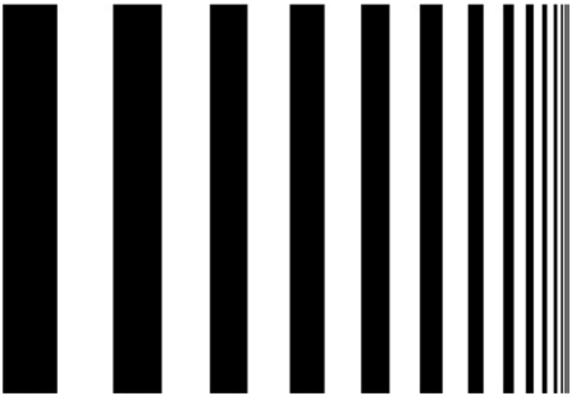

Fig. 7.2 A *black-and-white* variable-width *line pattern* used to determine the modulation transfer function

detector). The rows below (b–i) show an increasing signal blur (real detector) in conjunction with decreasing contrast and a decreasing MTF (j).

The reason for a detector to not be able to fully reproduce such line patterns with razor-sharp edges in the image is the spreading or blurring of the signal inside of the detector. The photographic film, the imaging plate and the scintillator/fiber optic/CCD array they all exhibit the inherent scattering events of electrons and photons. Accordingly, one single electron (and the ensuing photons), which enters the detector at one single point, excites not only one single pixel or grain but the signal spreads to neighboring pixels and grains too. This behavior can be expressed by the Point Spread Function (PSF), which describes the response of the detector to a single incident electron or photon—the input signal gets convoluted with the detector response, producing the output signal. If one were to illuminate one single pixel or grain with one single electron one could directly determine the PSF. However this method is extremely challenging. Two more manageable approaches are to follow the sharp knife-edge method or the noise method. Both methods assume that the PSF is independent of the position of the pixel in the array.

The knife-edge method requires placing a very sharp metallic edge across of the detector area. The material should not permit electron transmission. The resulting input signal into the detector can therefore be described by a step-function. However, the detector output signal shows a blurred edge in the image. Note though, that the knife-edge method has one-dimensional character—just like the step-function—not allowing determination of the PSF in the other lateral direction (along the knife-edge). Hence, a Line Spread Function (LSF) is used instead of the PSF. The LSF can be determined as the first derivative of the step function, or from the experimental edge profile, the edge spread function (ESF).

$$LSF = \frac{d}{dx} ESF(x) \approx \frac{\Delta ESF}{\Delta x} \tag{7.2}$$

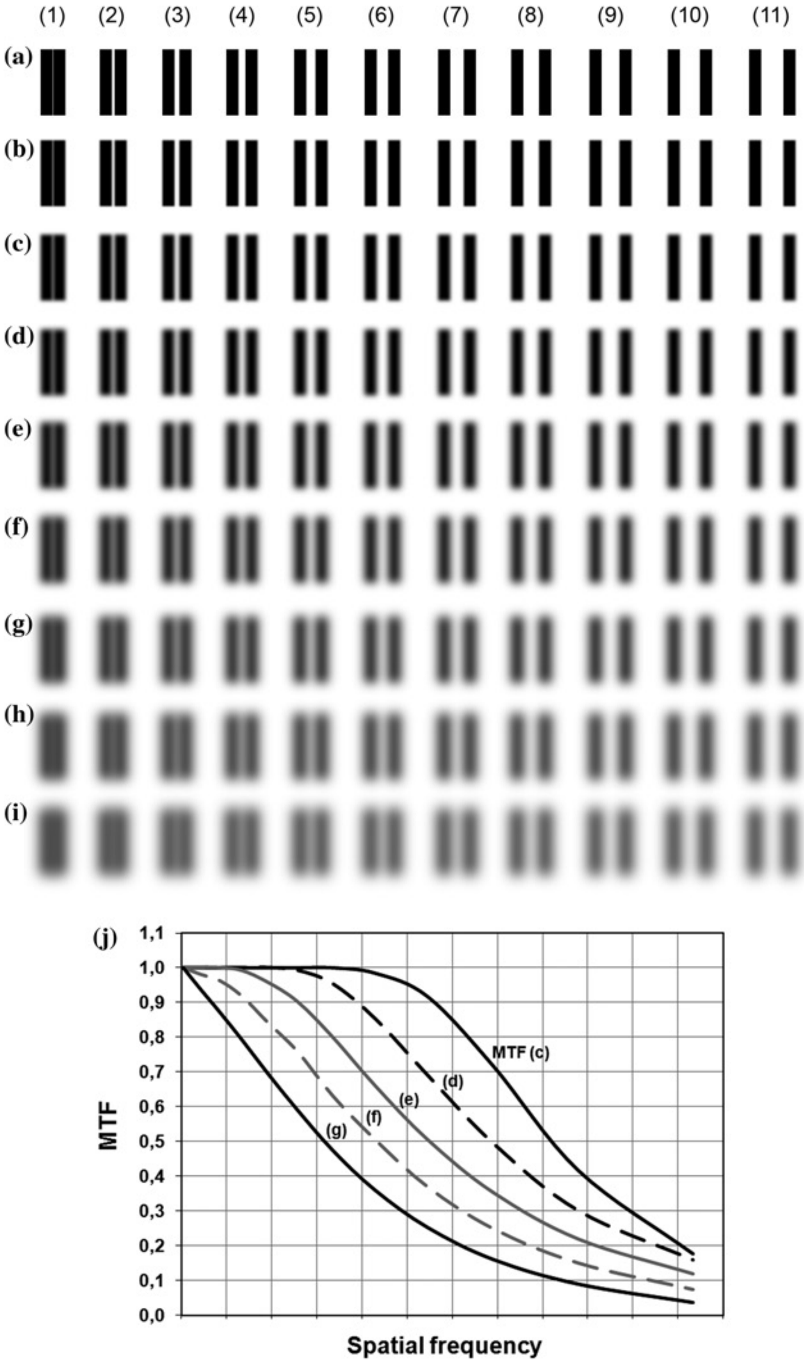

Fig. 7.3 Image simulation of the effect the MTF has on features in the image. Row **a** shows the unaffected image (perfect detector), rows **b**–**i** demonstrate increasing blur, **j** depicts the corresponding MTF graphs used for the image simulation

The ESF is determined by recording the knife-edge image, averaging over each line (or column) of pixels that runs parallel to the knife-edge and normalizing. The ESF cannot be differentiated analytically, hence the finite difference method applies.

Unfortunately, direct differentiation of the experimental edge profile has shown to be too noisy for a decent assessment of the LSF. Alternatively, a fitting procedure can be employed. The analytical approach to the LSF is by superimposing Gauss functions. The ideal input signal (perfect step function) is then convoluted with this analytical LSF and the result is compared to the experimental output signal. Variation of the free parameters of the Gauss functions allows adjusting the analytical LSF to match the experimentally measured LSF. The LSF corresponds to the PSF only under the condition that the PSF has rotational symmetry. However, in a real detector the PSF can be anisotropic. In photographic film this effect is known as Eberhard effect [2]. However, once the PSF (or the LSF) has been determined experimentally, the MTF is acquired by taking the Fourier transform of the PSF (LSF).

The issue of the noisy edge function and therefore a rather ineffective LSF can be explained by the metallic knife-edge causing stray X-rays and diffracted electrons right at the edge that can reach the detector where it should not be illuminated. This effect contributes to the artificial blurring of the edge that is independent of the detector response. Thus, the knife-edge method tends to overestimate the spreading of the input signal. On the other hand, inserting a sample into the electron beam might just as well introduce this type of edge blur—obviously, depending on the material composition. While the knife-edge is supposed to be inserted right above the detector to minimize such scattering effects, the sample is usually inserted at a much higher position along the electron beam. Thus, minute scattering along, for example, the ion-milled hole in the sample or any thicker section, and which may be regarded as considerably less scattering than the knife-edge, can cause similar effects in the image, which is recorded at a much larger distance. Thus, it remains debatable, whether or not it is better to de-convolute an experimental image (with sample) with an MTF that was acquired without image distorting scattering, than using an MTF that was captured with a possibly more realistic experimental scenario. Reproducibility and standardization of such distinct test methods are a challenge though.

An alternative to the knife-edge method to determine the MTF of a detector is the noise method. It requires a homogeneous illumination of the entire detector area. The number of electrons per unit time and unit area that reach the detector are Poisson distributed. An ideal detector would therefore have pixel/grains that are statistically independent (each a small individual detector, with no PSF effects) and the frequency spectrum of the noise could be expressed by a constant. This number would only depend on the variance of the noise in the image. In a real detector, however, the recorded homogeneous noise image requires a convolution with the PSF and the inherent detector noise (background noise, conversion noise) needs to be added.

$$\mathit{Noise\ image} = \mathit{Poisson\,noise} \otimes \mathit{PSF} + \mathit{detector\ noise} \tag{7.3}$$

Discrete Fourier Transformation (*DFT*) yields the frequency spectrum.

$$\begin{aligned} DFT\,(Noise\,image) &= DFT\,(Poisson\,noise) \times DFT\,(PSF) \\ &\quad + DFT\,(detector\,noise) \end{aligned} \tag{7.4}$$

where $DFT\ (PSF) =$ MTF, and $DFT\ (Poisson\ noise) =$ constant + noise.

As can be seen the PSF can be calculated by taking the Fourier back transform of the MTF. The constant is unknown and as such the result has to be scaled and normalized to unity under the assumption that for small spatial frequencies the MTF tends to unity. Averaging over the entire illuminated area allows minimizing the noise in the frequency spectrum. This can be achieved by first Fourier transforming and then averaging the noise line-by-line or column-by-column. This method also allows examining the rotational symmetry of the MTF and the PSF. Any additional inherent noise of the detector introduces only systematic errors to this method. Therefore, to minimize these errors one needs to record these noise images in a dose (intensity) range where the inherent detector noise is negligible compared to the noise of the input signal.

7.1.3.2 Detector Quantum Efficiency

The DQE is a most commonly used measure characterizing the overall quality of an imaging detector. Imaging quality is particularly affected by the combined effects of signal and noise performance expressed as a function of object detail—spatial frequency. In other words, it determines how well a detector can distinguish important low-contrast information from noise. This is of particular importance for low-dose applications, where the number of incident electrons is limited, e.g., due to sample radiation exposure limits, and resulting beam damage. Figure 7.4 demonstrates how image contrast and noise interplay.

Any signal inherently comes with its noise spectrum—call it shot noise, which should be Poisson distributed. An ideal detector registering such signal under perfect imaging conditions, will transfer that signal (and its noise) to the read-out end without adding any further noise (background noise) to the signal—hence, it has a DQE $= 1$. However, in practice the detector background and/or conversion noise will cloud the true signal, making it difficult, for example, to clearly discern very small features of interest in the image. A detector cannot increase the true signal, but it always adds noise—consequently, it has a DQE < 1. Background and conversion noise are inescapable in any digital imaging chain. Thus, image quality strongly depends on the often used Signal-to-Noise Ratio (SNR).

It is intuitive that without input signal there is only uniform background noise that can be displayed. Increasing the signal to, for example, a few electrons (or photons) may by far not suffice to allow distinguishing the signal from the background noise either. Increasing the signal more and more may result in a threshold signal strength that will eventually permit distinguishing the signal from the background noise. There are a number of threshold values of what the minimum SNR needs to be for the signal to qualify as a ‘true’ or ‘good’ signal. SNR numbers of 3:1 and 5:1

Fig. 7.4 Demonstration of how contrast and noise affect image quality

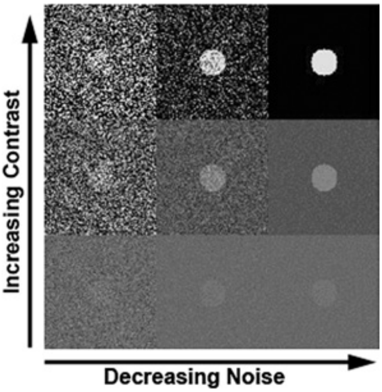

are very common ratios. Hence, the minimum number of incident electrons required to meet a specified SNR is a measure of a certain level of image quality. Knowing (ideally) also the noise level that was involved in this specific SNR allows determining the number of incident electrons that would have been sufficient for this image quality level if the noise had been non-existent—in essence the number of equivalent incident electrons, K. Relating K to the actual number of incident electrons, q, that were used to record an image with specified SNR defines the DQE

$$DQE = \frac{K}{q} \tag{7.5}$$

In the ideal case where noise is non-existent, $K = q$ and the ideal detector is characterized by DQE = 1. A real detector, as mentioned above, will have DQE < 1. In other words, the DQE describes how good a real detector represents the true image information relative to the ideal detector.

Experimentally, it is a challenge to determine both K and q with high accuracy. Even with very sensitive electron current measurements in the pico-Amp range, 1 pA still corresponds to over 6 million electrons, and at this level the measurement error is as large a the value measured.

Alternatively, the DQE can be expressed as [3]

$$DQE = \frac{SNR_{out}^2}{SNR_{in}^2} = \frac{\left(\frac{I_{out}^2}{\sigma_{out}^2}\right)}{\left(\frac{q^2}{\sigma_{in}^2}\right)} \tag{7.6}$$

relating the signal-to-noise ratios of the output to the input signal. However, in this form care is advised as this equation is only valid if the input signal corresponds to a uniform Poisson distribution. In the second expression I_{out} is the detector read out count rate, q the number of incident electrons (as before), and σ_{out} and σ_{in} are the respective variances. Assuming uniform Poisson distribution, $q = \sigma_{in}^2$ simplifying (7.6) to

$$DQE = \frac{I_{out}^2}{q\sigma_{out}^2} \tag{7.7}$$

Further simplification can be arranged by considering the conversion rate, c. Each detector system associates a count rate (usually counts per second) to a specified number of incident electrons (or electron intensity). That count rate is what the detector displays, for example as a pixel value (or grey scale value). The conversion rate, c, is therefore defined as the count rate per incident electron.

$$c = \frac{I_{out}}{q} \tag{7.8}$$

A CCD-based electron detector allows determining and adjusting this conversion rate at the A/D converter. Depending on the detector manufacturer conversion rates vary between 5 and 50. Combining (7.7) and (7.8) gives

$$DQE = c\frac{I_{out}}{\sigma_{out}^2} \tag{7.9}$$

Remember that adjacent pixels cannot be considered as completely isolated from each other and that the PSF tends to spread the incident image information over a few neighboring pixel. This results in a noise-leveling operation. The input noise may therefore be higher than the output noise, causing an unrealistic DQE > 1. This error can be compensated by introducing a mixing factor [4]

$$\sigma_{out,\,comp}^2 = \frac{\sigma_{out}^2}{m} \tag{7.10}$$

which is defined as [5]

$$m = \frac{1}{N^2}\sum_{i=1}^{N}\sum_{j=1}^{N} MTF_{i,j}^2 \tag{7.11}$$

where N is the number of pixels in one dimension. This mixing factor is independent of the incident dose. For an ideal detector $m = 1$, whereas for a real detector $m < 1$. Therefore, (7.9) needs to be amended

$$DQE = c\frac{mI_{out}}{\sigma_{out}^2} \tag{7.12}$$

The above equations allow determining the DQE experimentally by selecting a specified region of interest, for example, 512 × 512 pixel taken from noise images recorded under varying electron intensities.

With

$$I_{out} = \frac{1}{512^2}\sum_{i=1}^{512}\sum_{j=1}^{512} I_{i,j}$$

and

$$\sigma_{out}^2 = \frac{1}{512^2}\sum_{i=1}^{512}\sum_{j=1}^{512}\left(I_{i,j} - I_{out}\right)^2 \tag{7.13}$$

and (7.11), one can experimentally determine the DQE using (7.12).

Note, that the mixing factor, *m*, introduces the MTF into the DQE equation. This allows a direct correlation of the DQE with the spatial frequencies in the image. In other words, if a sample is viewed under the same contrast and detector noise conditions, large features of the sample can be deciphered easier than small features in the recorded image. This makes the DQE a rather important parameter, more than for example, the spatial resolution limit of a microscope. Even if a microscope can in theory resolve features on the sub-nanometer scale, one cannot take advantage of those resolution capabilities if the detecting system has low DQE, which prevents recognizing very small objects in the image. Consequently, high DQE (i.e., high SNR) or low system noise is therefore key to capturing the greatest portion of useful image information. Often, the only way to compensate for poor SNR is to increase radiation dose, which is for many applications an unacceptable trade-off.

There is a connection between DQE and CCD pixel size. Generally, the larger the pixel size the better the SNR. This is because the input signal is much better converted into output signal in a large pixel, while the pixel noise remains constant. A minimized PSF also contributes to this improvement as the incident electrons—although scattering inside the larger pixel as much as before—do not cause a spreading of the incident signal over a number of neighboring pixels. As a logical consequence, CCD-based electron detectors should preferably display large pixels. However, from the spatial resolution point of view small pixels are better suited for high-resolution imaging. Hence, a careful evaluation of application requirements is mandatory when designing an imaging detector. There is a point of diminishing return: while noise remains constant in a given detector system, the amount of useful signal captured per pixel dwindles with decreasing pixel size. As a result, the finer the pixel matrix, the lower the SNR at each pixel. This, combined with the lower inherent contrast of small objects will limit detectability and visualization. Determining the optimum balance between pixel size and noise is therefore crucial to the development of CCD-based electron detectors.

The ideal case of single-electron recording can be best achieved with large pixels (>100 μm). Capturing electron after electron, suitably spaced in time as they arrive at the pixel and are read out individually before the next electron enters the pixel is the best for single-electron detection, because the SNR is optimized under such conditions. The draw back of miserable spatial resolution with such large pixels can be overcome by employing algorithms designed to back-track the trajectory of the electron to its point of entry into the pixel. These algorithms rely on scattering simulations and center of gravity determination of the 'scattering cloud' and the energy deposited by the electron. This method works only if the scattering cloud covers two or more pixels. Equipped with such algorithms one can virtually reduce the pixel size to <10 μm and thus have a more accurate positioning of the electron in detector-space. However, in real electron imaging more than just one electron at a time is registered by each pixel. Already two incident electrons will make the back-tracking and positioning algorithms infinitely more difficult to handle. Any large number of electrons will render this back-tracking approach highly impractical, if not impossible when considering that normal electron imaging deals with electron numbers, per pixel, per exposure (<500 ms) in the 10^6 range.

7.1.3.3 Dynamic Range

The dynamic range of a detector is defined as the range between the largest and smallest possible values of a variable quantity—in this case the number of electrons that a detector can register. This range should be as large as possible, from a single electron to several millions of electrons in one and the same image—a condition encountered for example in diffraction patterns. For the CCDs behind the scintillators that convert electrons to light, the dynamic range of such CCDs is many times less than that of the human eye (in the visible spectral range). Assessing the dynamic range for film with electrons is difficult, due to the ambiguity on how to determine the minimum and maximum detectable signals. For CCD-based electron detectors the minimum is certainly determined by the readout noise of the detector.

7.1.3.4 Linearity

The linearity of a detector is generally determined by recording images of uniform illumination and plotting detector readout (counts) as a function of electron intensity (electron dose). However, the difficulty lies in accurately determining the electron intensity on both the high- and low-dose end. Linearity is important when intensity variations are to be determined as is the case for structure factor determination.

7.1.3.5 Uniformity

The uniformity of a detector measures the gain variations among different pixels. Examining the raw data (pixel values) of an image that was recorded under uniform illumination will reveal that there are large variations in the readout signal among pixels. As every pixel has its own readout pathway each one will therefore exhibit unique conversion and gain characteristics. It is not unusual with CCD-based electron detectors that neighboring pixels differ by a factor of 10 in gain, thus, the almost identical incident signal (considering the PSF effects) results in a pixel that may be ten times brighter (or dimmer) than its neighbor. On a larger scale, this behavior can even manifest in entire detector areas that respond stronger than other areas of the detector to the identical uniform illumination. The ideally uniform image may now look as if it were displaying stains.

Similar gain variations but not as distinct, applies to film and the imaging plate. Variations in gain depend here on the phosphor grain morphology and orientation relative to the incident electron that may cause stronger or weaker scattering events inside affecting energy deposition and structural changes (silver halide to silver conversion). Regardless of random grain orientation and a homogeneous distribution, neighboring phosphor grains may differ significantly in their response to electron irradiation.

In CCD-based electron detectors this non-uniformity can be corrected for by averaging over many images recorded with the same uniform illumination. This primarily levels out gain variations over time within each pixel but not among neighboring pixels or any other pixel in the detector area. The average image gain, $\bar{g}_{img}$, is calculated according to

$$\bar{g}_{img} = \frac{\bar{I}_{out} - \bar{b}}{\bar{N}_e} \tag{7.14}$$

where $\bar{b}$ is the average background noise and $\bar{N}_e$ is the averaged electron dose per pixel. The gain variations among all pixels are reduced by taking the average pixel gain and dividing it by the average image gain.

$$\gamma(n) = \frac{\bar{I}_{out}(n) - \bar{b}(n)}{\bar{N}_e \bar{g}_{img}} = \frac{\bar{I}_{out}(n) - \bar{b}(n)}{\bar{I}_{out} - \bar{b}} \tag{7.15}$$

7.1.3.6 Resolution and Pixel Size

For a discrete 2-dimensional detector the spatial resolution obtained in the image is solely determined by the pixel size. However, in practice a detector's spatial resolution is determined by the PSF as discussed before, and not simply by the detector pixel size. The problem arises when the PSF extends as much as 70–90 μm FWHM—as generally obtained in commercial CCD-based electron detectors. In light of that, all efforts to improve the spatial resolution in the image by reducing the pixels size as much as technically possible (standard pixel size is currently 14 μm, with some detectors having 5 μm pixels) will not be as successful as expected. As long as the PSF extends beyond the pixel boundaries and cannot be confined to it, the PSF will be determining the spatial resolution. Numerous optical elements and interfaces as encountered in CCD-based electron detectors contribute to signal spreading and a broad PSF. However, knowing the particular PSF of a detector allows deconvoluting each image, and in return improving the spatial resolution in the image. This possibility explains why it is not customary to settle for pixel sizes as large as the PSF for a specific detector.

As mentioned already at the end of Sect. 7.1.3.2, pixel size has to be carefully chosen, depending primarily on application. Single-electron and ultra-low-dose applications will benefit from large pixels and their improved SNR characteristics. Instead, regular and high-dose applications will most likely not benefit from large pixels because of the lack of spatial resolution in the image.

7.1.4 Comparison of Electron Detectors

The following section will present a few results of those critical detector characterization parameters for the 'conventional' electron detectors. Figure 7.5 shows

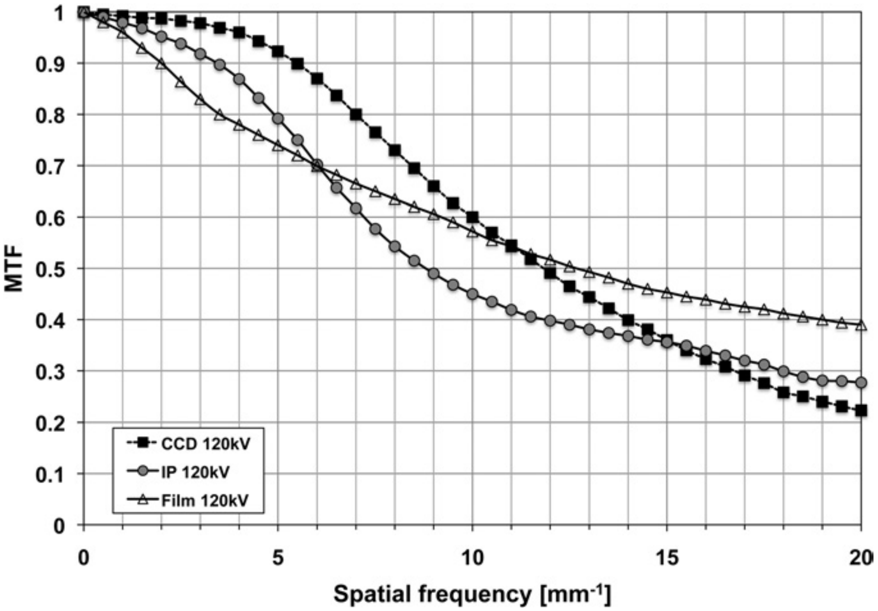

Fig. 7.5 The MTF is plotted as a function of spatial frequency, f, for photographic film (Kodak 4463), an image plate (Fuji IP25), and a CCD-based electron detector (Gatan 679 with YAG scintillator). The noise method was used for the determination of the MTF

the MTF plotted as a function of spatial frequency, *f*, for photographic film (Kodak 4463), an image plate (Fuji IP25), and a CCD-based electron detector (Gatan 679 with YAG scintillator). The film has the typical 3 μm silver halide grains, whereas the pixels sizes of the image plate and the CCD-based electron detector are 25 and 24 μm respectively. Consequently with 25 μm pixel, the MTF shown here is limited to the frequency range 0–20 mm^{-1}—up to the Nyquist frequency of the image plate, which is defined as $f_N = 1/(2 \cdot \text{pixel size})$. Furthermore, the regions of interest in all three detectors were chosen to be 1024×1024 pixel (grains) in size.

The noise method was used for the determination of the MTF. However, due to the sensitivity of this method to inherent background noise, and in the attempt to reduce the negative effects caused by background noise, the MTF was determined in the medium- to high-dose range for the CCD-based electron detector and the photographic film, while the image plate was analyzed using low-dose electrons. Remember that reproducibility and standardization of such distinct MTF test methods are a challenge. The described methods of analysis used for determining the MTF of a detector, especially their computational aspect may vary only little in their approach, but may produce considerably different looking graphs. Although a uniform and consistent analysis method is everybody's aspiration and intention, differences in, for example, the Gauss fitting parameters, the line and/or column averages, and especially the order in which these separate steps are applied to the data set can make a significant difference in the outcome. Thus, in publications

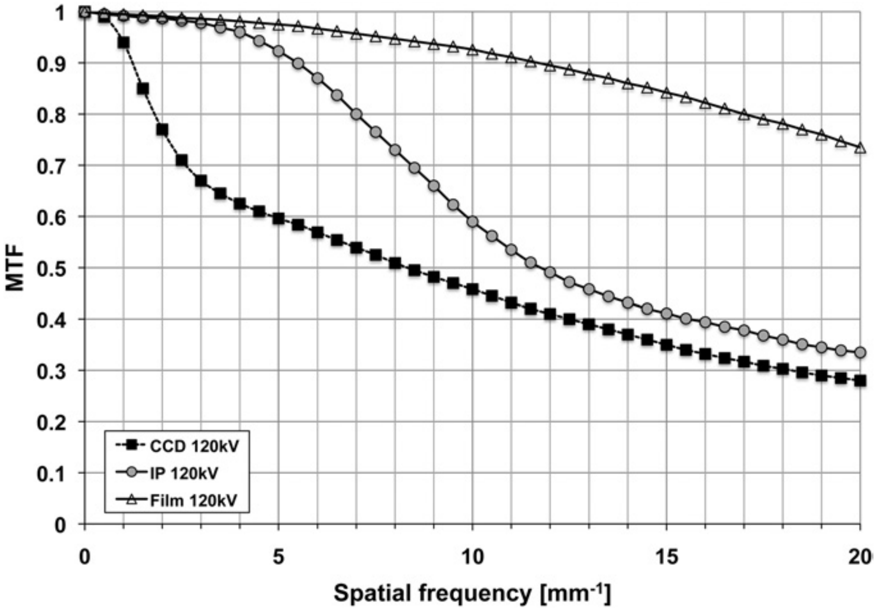

Fig. 7.6 Alternative MTF graph, plotted as a function of spatial frequency for film, image plate, and CCD-based electron detector

one can find MTF graphs as presented in Fig. 7.5, but also MTF graphs (even of the same detector) that look like the graph shown in Fig. 7.6.

The MTF graph displayed in Fig. 7.5 shows how the difference between the three detection systems can be minimal over a wide range of spatial frequencies. Only at low spatial frequencies, the CCD-based electron detector is performing better than the other two detection systems, whereas at high spatial frequencies the photographic film is transmitting information better, i.e., 0.38. The MTF of all three detection systems in this high spatial frequency domain agree well with other publications [6–8] where CCD-based electron detectors achieve MTF values of 0.22–0.28, and imaging plates are slightly better with 0.27–0.33.

Alternatively, Fig. 7.6 shows how the CCD-based electron detector now relays the least amount of information, whereas the image plate and the photographic film are better in this regard [9]. Across the entire range of spatial frequencies the photographic film is the best recording media. Film still transmits 0.73, i.e., 73 %, of the original signal at 20 mm^{-1}, whereas the image plate and the CCD-based electron detector transmit only 0.34 and 0.28 respectively. The value for the CCD-based electron detector and the image plate at 20 mm^{-1} agrees well with what is presented in Fig. 7.5, however, the shape of the curve and its behavior at low spatial frequencies is considerably different.

Transmission of information at high spatial frequencies is generally desirable for high-resolution electron microscopy work, so the MTF behavior of the detection system is of significant interest there.

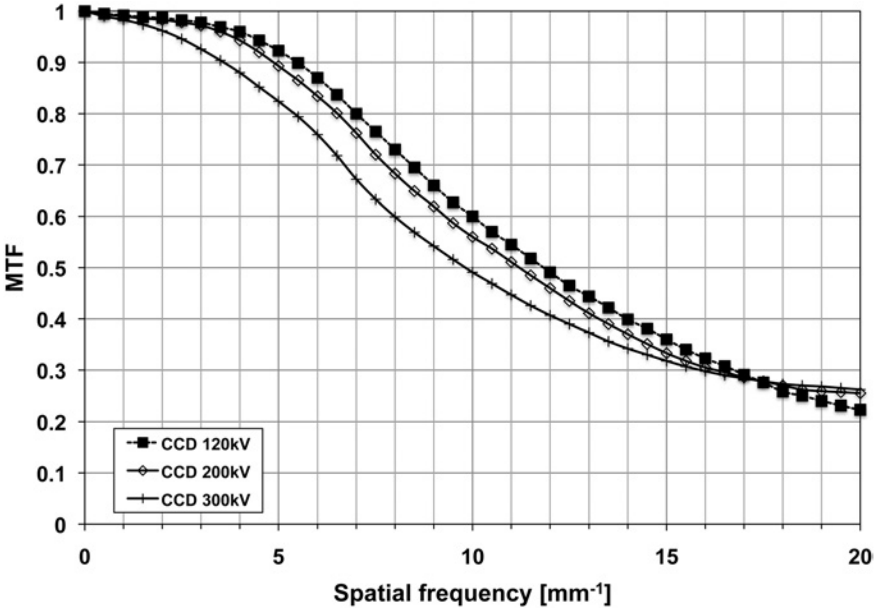

Fig. 7.7 The effect of electron acceleration voltages on the MTF

The effect of electron acceleration voltages (120, 200 and 300 kV) on the MTF is shown in Fig. 7.7. The MTF tends to be better at lower acceleration voltages, especially at the low-spatial frequency end. The reason for this behavior is the diminished scattering of the incident electron in the scintillator and therefore the signal is spread less over the fiber-optics and the ensuing pixels.

Figure 7.8 shows the DQE of these three detector types. The DQE is shown as a function of electron dose in terms of electrons per unit area (μm^2), because the pixel and grain sizes differ. Furthermore, it is a double logarithmic graph. The DQE of the CCD-based electron detector exhibits a fairly high and level DQE in the medium- to high-dose range with values around 0.45–0.55. This relatively high DQE for CCD-based electron detectors agrees well with other published investigations [5, 6]. The DQE however decreases to <0.2 in the low-dose range, i.e., at less than 0.006 e/μm^2, which is caused by the inescapable background noise in the CCD that becomes predominant at low electron doses.

The imaging plate and film show larger variations. The imaging plate has a high DQE in the low-dose range, 0.4, and decreases in the medium- to high-dose range to levels below 0.07. This is due to the conversion noise that increases considerably with electron dose. Film instead, shows a decent DQE only in the medium-dose range, 0.38, and drops off steeply at high and low doses. The general shape and position of the DQE for film can be manipulated (within narrow limits) by varying the film development parameters. The results agree with the observation that a CCD-based detector with high DQE can improve one's ability to distinguish

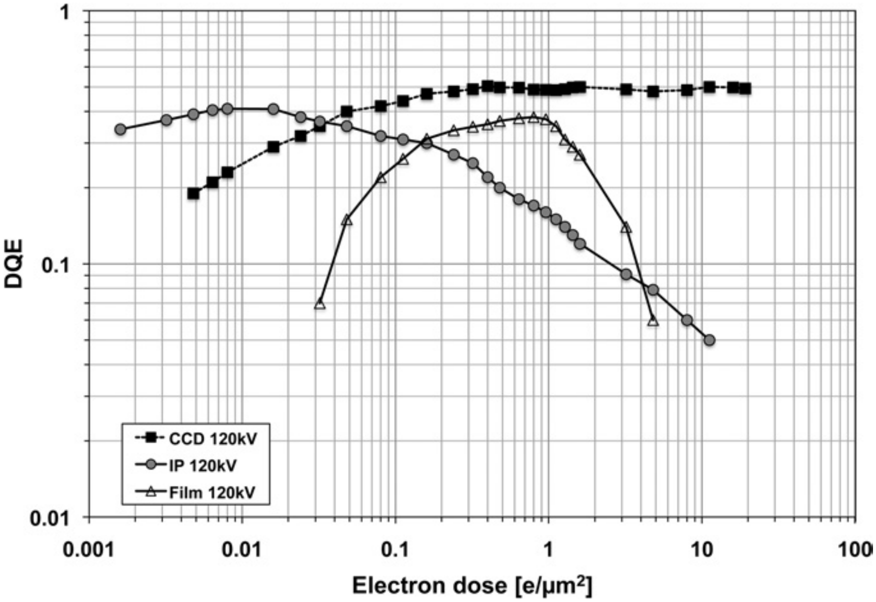

Fig. 7.8 DQE of three detector types, shown as a function of electron dose in terms of electrons per unit area (µm^2)

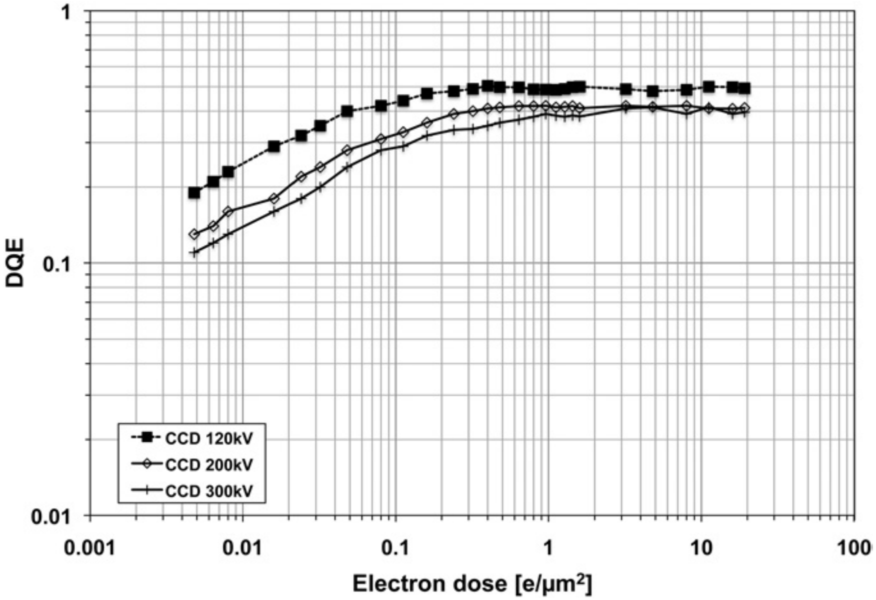

Fig. 7.9 The effect of electron acceleration voltages on the DQE

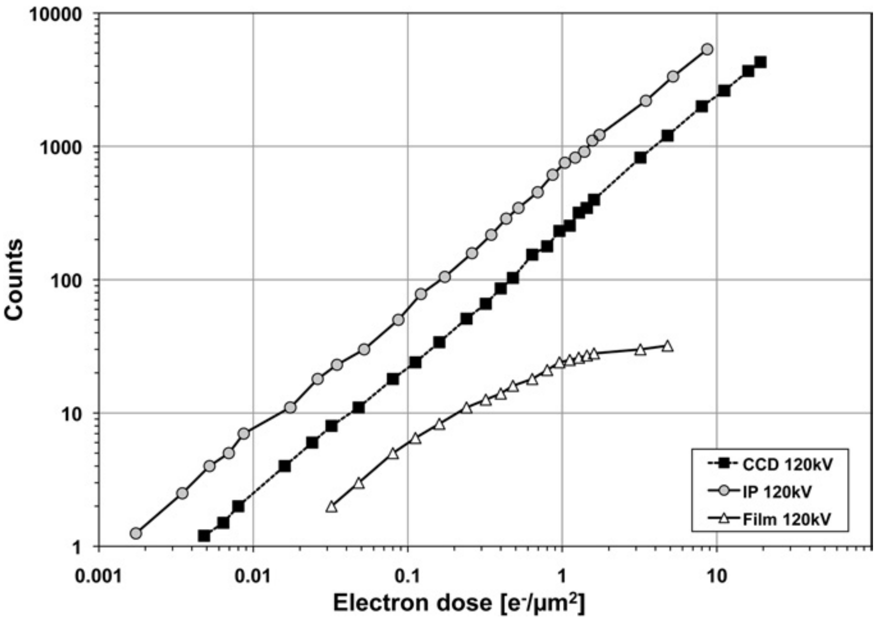

Fig. 7.10 The linearity of the three detector types: CCD based electron detectors, film, and image plate

small, low-contrast features from background noise—even though this high-DQE detector may have substantially inferior spatial resolution capabilities, i.e., significantly larger pixel size, than film.

Similar to the MTF, one can also notice an effect of acceleration voltage on the DQE performance of the CCD-based electron detector. Figure 7.9 shows how the DQE changes by varying the acceleration voltage (120, 200 and 300 kV).

Considering the dynamic range, and linearity: the CCD-based electron detector and the imaging plate make full use of their analog-to-digital converter that provides for 16 and even 32 bit. Film instead is limited to approximately 11 bit (depending on the film scanner). The linearity of the three detector types is shown in Fig. 7.10. Note the large scale of the electron dose (more than 10 e/μm^2, which translates to approx. 6000 e/pixel at 24 and 25 μm pixel size) that the CCD-based electron detector and the imaging plate can handle, while still exhibiting a linear response. Film instead is highly non-linear and not as a capable in handling large electron doses.

7.1.5 Direct Electron Detectors

As mentioned at the end of Sect. 7.1.2.3, the reason and motivation to further transition from the indirect to the direct electron detection techniques, is the prospect to finally operate an electron detector with all the digital and user-friendly advantages of the existing CCD based detector systems, yet with improved characteristics. The main driving force for these detector developments are the high-energy physics and the medical imaging communities. Therefore, the applications differ significantly as well as the type and energy range of the radiation (high and low energy electrons and X-rays).

Direct detection generally entails that the detector is directly exposed to the radiation source (electrons, X-rays, visible photons, ions, and other ionizing particles). Electron-to-photon conversion is not required anymore, which eliminates the problem of an extended PSF caused by optical interfaces within a CCD-based detector system (see Sect. 7.1.2.3). The direct exposure to the incident electron beam however poses a different set of challenges that need to be overcome, radiation hardness being the most 'damaging' problem.

7.1.5.1 The Active Pixel Sensor

The development of direct detections technique dates back as far as 1968 and 1969 [10–12], even before the CCD was invented in 1970 at Bell Labs. However, technical difficulties in the manufacturing process of direct detectors made the CCD more viable and applicable at the time. The direct detection techniques back then and today are all based on the Complementary Metal-Oxide-Semiconductor (CMOS) technology for designing and manufacturing integrated circuits (IC). In the 1990s the CMOS technology was in a better position to reliably manufacture ICs at smaller and smaller scales, allowing for the design of a direct detector that used intra-pixel charge-transfer possibilities [13]. These CMOS-based direct detectors are called Active Pixel Sensor (APS). The basic APS design and its functionality will be described in the following section. There are a large number of design possibilities and layout variations one could dive into—too many to cover them all in the limited the space provided here. Furthermore, many of these detector variations and designs are still in the prototype stages with extensive and costly development, improvement, and testing stages still ahead.

A CMOS type APS, designed to efficiently detect electrons, X-rays, and other ionizing particles, especially the low energy type of radiation, differs from any other standard CMOS imaging sensor. The critical parameter is the thickness of a p-epitaxial layer that determines detector sensitivity. A very thin layer allows only very few secondary electrons (electron-hole pairs) to be created via scattering events of the primary, incident electron, causing a very shallow junction depth, and consequently the amount of collected charges inside the sensing layer is limited. As a result the signal-to-noise ratio (SNR) of such a detector is poor. Increasing the epitaxial layer thickness improves the SNR significantly.

Figure 7.11a demonstrates in a schematic cross section of the detector the working principle of the direct detection mechanisms. It shows how an incident, primary electron creates secondary electrons through scattering events along its path throughout the entire layered structure of the detector. The $p{+}{+}$ bulk layer is

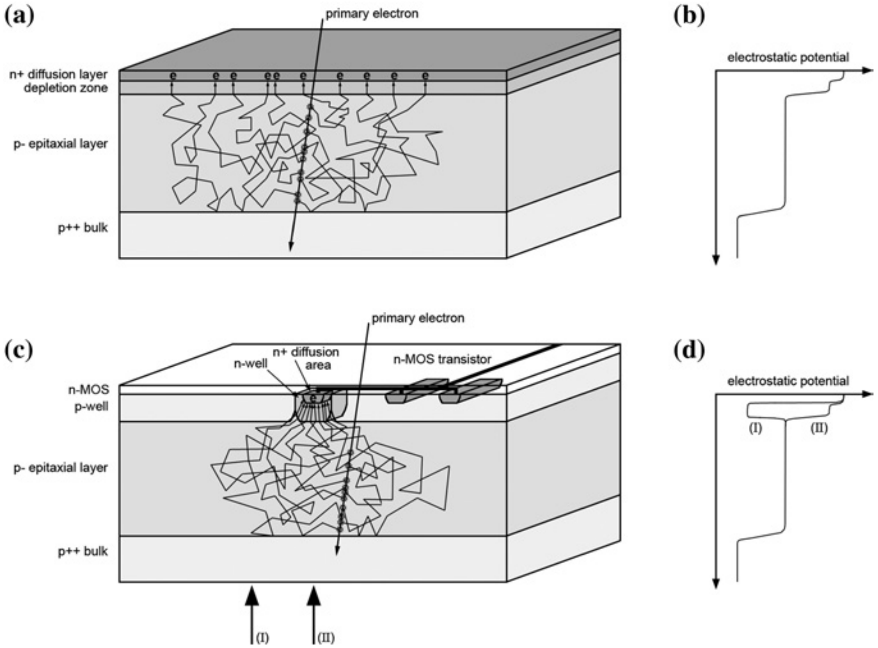

Fig. 7.11 A schematic cross section of (**a**) a CMOS detector and (**b**) an APS detector, depicting the working principle of the direct detection mechanism. **c** and **d** show their respective electrostatic potentials

a highly doped standard silicon wafer that acts as support structure. A *p*-epitaxial layer is grown on top of the substrate and is the key feature because it is an integrated epitaxial silicon layer (purer silicon of higher resistance) that acts as the sensing component of a detector. On top of that is an $n+$ diffusion layer, which is added as a standard practice in normal CMOS processing. A depletion zone is formed at the interface between the $n+$ diffusion layer and the *p*-epitaxial layer, which is equivalent to an $n+/p-$ diode. This layered structure creates internal electric fields and potential barriers and gradients that allow manipulation and guiding of the secondary electrons. For example, the interface between the $p++$ bulk and the *p*-epitaxial layers create an electric field barrier that reflects secondary electrons back into the epitaxial layer, preventing them from entering the $p++$ substrate. In contrast, in the epitaxial layer there is no electric field, and secondary electrons inside tend to diffuse following a rather random path until they reach the depletion zone. Once inside the depletion zone the secondary electrons experience the electric field of the $n+$ diffusion layer, causing them to drift (rather than to diffuse) into the $n+$ diffusion layer and remain trapped inside its deep potential well. Figure 7.11c depicts the electrostatic potential of such a layered structure as shown in Fig. 7.11a.

The presented concept can be utilized and adjusted to create a highly sensitive sensor, capable of single electron detection. It can also be extended to incorporate the read-out circuitry into the sensor—effectively creating an APS. A schematic cross section through an APS is shown in Fig. 7.11b. The sensor structure shows a similarly layered configuration as before, but also displays the incorporation of additional structures, especially at the top. The $p{+}{+}$ bulk substrate is the same, and the p-epitaxial layer is thicker than before (not shown in schematic, Fig. 7.11b as it is not to scale), but on top of the epitaxial layer comes a p-well layer with inclusions of lightly doped n-well zones. The former $n+$ diffusion layer is now reduced to small $n+$ diffusion spots within the n-well zones. A depletion zone as before is not specifically shown anymore, but exists in reduced size at the interface between the n-well and the p-epitaxial layer. This configuration is now representing a small diode junction placed in direct contact with the epitaxial layer, and thus capable of collecting all secondary electrons. To enhance electron collection at the small diode and to make the entire epitaxial layer volume and as such the entire pixel surface area sensitive to incoming radiation, the n-well and $n+$ diffusion area is surrounded by p-well structures that reflect the secondary electrons just like bottom $p{+}{+}$ bulk substrate does, helping to confine and guide the secondary electrons toward the small diode junction. These confining and guiding potential barriers are due to the doping level of the epitaxial layer, which is lower than that of the surrounding p-well structures and the $p{+}{+}$ substrate, and they are of height [14]

$$V = \frac{kT}{q} \ln \frac{N_{sub}}{N_{epi}} \tag{7.16}$$

where k is the Boltzmann constant, T is the absolute temperature, q is the electron charge, and N_{epi} and N_{sub} are the doping levels of the epitaxial layer and the substrate, respectively.

An additional benefit of the p-well structures is that they shield the embedded n-channel transistors from the diffusing secondary electrons. Figure 7.11d shows the electrostatic potential at positions (I) and (II) through the cross section of the APS.

The n-channel transistors embedded in the p-well structures and the metallic contacts constitute the on-sensor readout and control electronics. The layout of these electronic components allows for a large variety of configurations. Here, only three basic and very common configurations are shown in Fig. 7.12a–c.

The first one (Fig. 7.12a) represents the very basic version, a Passive Pixel Sensor (PPS), that includes just one single transistor, which multiplexes the collected charge for readout. The layout is very simple and compact, but because it is unbuffered it brings about a slow readout and a poor SNR. The second circuit layout (Fig. 7.12b) represents a standard APS with three transistors (buffering, multiplexing and resetting), resulting in a faster readout and better SNR. Figure 7.12c shows an APS with an additional fourth transistor and a capacitor that can be used for either a shutter function or a sample-and-hold function.

Typical dimensions of these APS layers and structures are: 12–16 µm epitaxial layer thickness, 3 µm square diode, 20 µm square pixel with between 1 and 4

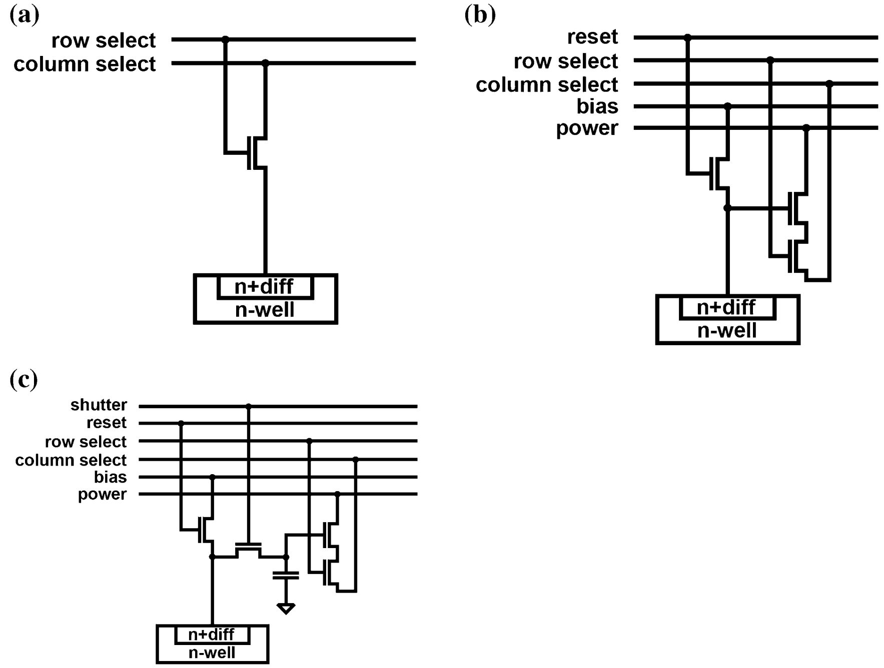

Fig. 7.12 Electric diagrams of three direct detector types, (**a**) a Passive Pixel sensor (PPS), (**b**) a standard Active Pixel Sensor (APS), and (**c**) an APS with additional functionality

diodes. The 4-diode arrangement is expected to reduce charge spreading between neighboring APS pixels. Charge spreading to neighboring pixel is an undesired effect, because it reduces spatial resolution in the recorded image in an identical manner to the CCD-based electron detectors where the signal spreads due to the internal optical interfaces. Unfortunately, the thickness of the epitaxial layer strongly affects this performance. Increasing the epitaxial layer thickness not only increases the number of generated secondary electrons, but it also allows for charge spreading and it increases the collection time, which in turn affects the readout speed. Another structural parameter that needs to be considered when designing an APS is the depth of the *n*-well zone, as it affects charge collection time. Furthermore, the fill-factor—the ratio of radiation sensitive area to the total area of the pixel—is important. If the electronic circuitry is covering too much surface area of the pixel, it hampers the penetration of primary electrons into the sensitive epitaxial layer. Remember, that for example 300 kV electrons cannot penetrate through samples that are more than 400 nm thick (a typical value for metals), without being severely diverted off the their initial direction of travel—hence becoming useless for TEM imaging purposes. Some of the incoming electrons are absorbed in that 400 nm thick sample, while the rest will exit the sample, but will have lost a significant amount of the energy. The "cloud" of secondary electrons instead can reach much farther into the sample (or detector in this case) and as such the scattering volume is much wider and much deeper than the primary electrons may be able to reach. Hence, covering the surface area of the pixel with circuitry that measures a few micrometers in thickness will make it difficult for the primary electrons to reach the epitaxial layer, whereas the secondary electron cloud may well reach into the epitaxial layer, but generating a weaker signal. X-rays and other ionizing radiation have different penetration depths—again, a clear indication, that the detector requires appropriate design depending on the application.

From the operational aspect, the readout and data handling options are also affecting the performance of an APS. Whether or not the APS pixels in a detector array are reset before each readout (individually or row/column-wise) affects SNR. Increasing the integration or collection time improves SNR.

The bottom line is that detectors with APS offer a large number of parameters that can (and need to) be tuned to the respective application to achieve optimum performance. And it is certainly understandable that most of the current research into APS detectors concentrates on how to improve sensitivity and the SNR, especially for low-energy and low-intensity applications [15–28]. Less research is dedicated to the following problem: radiation hardness [29–32].

Some applications for these APS detectors can be demanding, requiring further development, re-designing and adjustment of current APS detectors. One experimental condition found in numerous investigations is high-intensity and/or high-energy radiation. Such experimental conditions can be detrimental to the APS detector. Damage to the detector can occur in a single, first exposure or over a slightly longer period of time (hours, days, weeks). Therefore, for such applications an APS detector needs to be radiation hard. It has been observed in many APS prototype test experiments that the electronic circuit on top of the APS gets damaged and malfunctions after a short period of time of being exposed to the incoming radiation. The degrading effect is associated with interface charges that hamper detector sensitivity and functionality. One has to remember, that scientists that are primarily interested in the outcome of the experiment may not think about the detector radiation hardness. The radiation source and its intensity may be intentionally selected to destroy the sample in a single, short exposure. In fact, the objective of the experiment may be to observe damage mechanisms. However, what the radiation source can do to the sample it can also do to the detector. In diffraction experiments, for example, there is little one can do to protect the detector from the central, highly intense beam. The only solution here is to manufacture a detector with a hole in the middle, where the damaging central beam can just pass through (and hit a Lead shield behind the detector). In this case, only the electrons that are scattered in the sample are reaching the detector as their path deviates from the central beam. Furthermore, fractions and pieces of the destroyed sample (even in the micrometer size range) that get propelled towards the detector during exposure to the intense incoming radiation can cause physical damage to the detector.

A solution for less intense incoming radiation, which nevertheless may still create damage over time, is to have the detector back-side illuminated. So far the APS detector described here was illuminated from the front, where the circuitry is located. Inverting the detector and removing the p++ substrate (this process is called back-thinning) such that the epitaxial layer is directly exposed to the incoming radiation, opens up another avenue for detector protection and making it radiation hard. The control and readout circuit is now at the back end of the detector and not anymore in the direct "line of radiation fire". For damage to occur to the circuit, the incoming radiation has to traverse the entire epitaxial layer and still possess enough energy to damage the circuit. Depending on application one can increase the epitaxial layer thickness to avoid incoming electrons reaching the backside of the inverted APS (circuit side) altogether. Figure 7.13 shows schematically how an APS detector undergoes back-thinning.

This back-side illumination idea was initially conceptualized to improve sensitivity and SNR, especially for low-energy applications (3–30 kV). As mentioned above, such low-energy electrons would not reach the epitaxial layer if the pixel surface is covered with p-wells and $n+$ diffusion structures a few micrometers in thickness. Even if they were to reach the epitaxial layer, the number of electrons reaching that far and the few secondary electrons created would be too little to generate a sufficiently strong signal that surpasses the electronic background noise within each pixel.

There is an alternative to the APS type of detector: the *pn*-CCD—or direct CCD—which is a detector based on the CCD working principle, but uses CMOS fabrication processes. While the APS sensor has all functions and all necessary transistors included within one pixel, a direct CCD has those functions remotely operating on a separate circuit board. CMOS image sensors offer superior integration, power dissipation and system size at the expense of system flexibility and image quality, especially in the low-dose range. In contrast, direct CCDs offer superior image quality in the low-dose range, and higher system flexibility, but at the expense of system size. The radiation damage discussed is a problem for APS detectors. In contrast, a direct CCD offers better radiation hardness, because there are no active MOS structures directly exposed to the incoming radiation, and the remaining structures can be designed to be fairly radiation hard.

7.1.5.2 The Direct CCD

The direct CCD comes close to many of the experimental requirements, yet further development is ongoing. To date, this detector performs such that the electronic noise is between 2–5 electrons (rms), frame readout speed is at 1100 frames/s, and single incident photon or electron events can be located to within 5 μm precision. The currently available pixel dimensions of 36–75 μm are optimized for high-speed readout and excellent signal-to-noise characteristics, however, for high-resolution multi-photon/electron imaging (i.e., multiple incidents in one pixel within one readout cycle) the pixel size needs to be reduced to 15–20 um. The concept of this direct CCD is based on a 450 um thick sensitive n-type Silicon layer, which can be fully depleted (sideward) by applying appropriate reverse-biased voltages to the *pnp*-structure from both the front and back of the direct CCD. Full depletion results in high detection efficiency, because the entire pixel volume is sensitive to radiation.

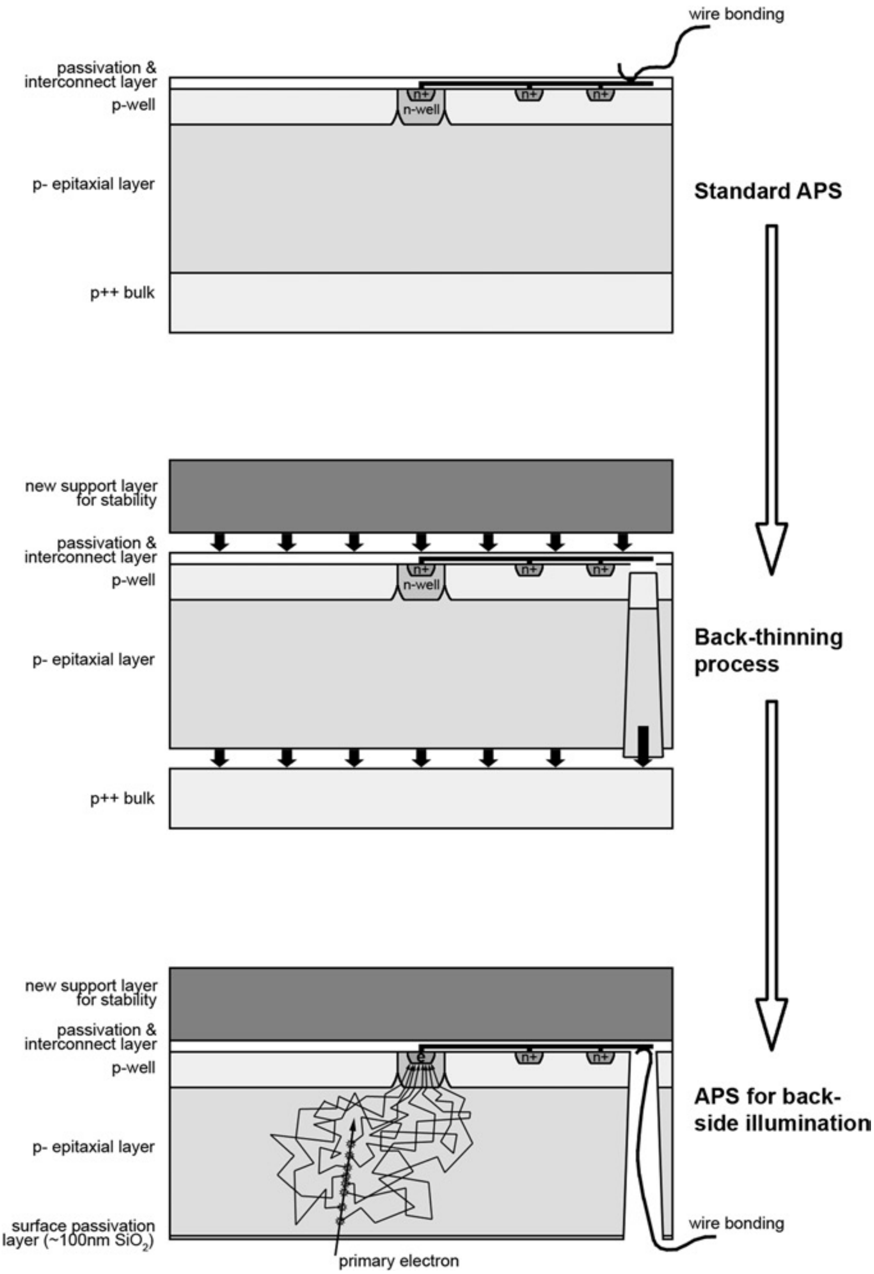

Fig. 7.13 A schematic explanation of the APS detector back-thinning process

By appropriately applying voltages to the *pn*-junctions a potential minimum close to the front surface is created, where electrons generated by the incoming radiation are stored. The pixel structure and transfer registers are created by ion-implantation on the front side, whereas a completely homogeneous and unstructured $p+$ implantation on the backside represents the entrance window for the incoming radiation. The rectifying *pn*-junction permits maximizing the electric field at the entrance window, which helps controlling the spatial spread of the charge cloud generated by the ionizing radiation within the pixel. The generated electron-hole pairs (secondary electrons) are then separated owing to their charge and the applied electric field. The electrons drift to their potential minimum, located within a layer of low resistance. During recording, i.e., the photon or electron integration time, the charges are stored within the potential well of each pixel, which is regulated by three transfer registers and two separate voltage levels. The stored charge in the image frame is then quickly transferred to the frame store segment—an adjacent section on the detector, with identical number of smaller and shielded pixels. The image frame can now be exposed again for the next image, while the frame store segment is read out row by row through the readout anodes of each channel of the CCD, amplified, shaped, processed and multiplexed by a dedicated analogue amplifier array, and transferred to an external computer for image processing. The external amplifier chip uses multicorrelated sampling for noise filtering. This chip also controls the detector sampling number, affecting so the detector noise and read out speed characteristics. The sampling number can be adjusted to meet specific experimental conditions. A high sampling number minimizes noise at the expense of read out speed, whereas a low sampling number increases detector speed.

7.1.5.3 Performance of a Direct CCD

A direct CCD detector has been employed on experiments using synchrotron X-rays, electrons, and photons in the visible and near-infrared domain [33–37]. Here, only some characteristics of the direct electron detection will be shown, taken from prototype experiments using a transmission electron microscope (TEM) operated at 100 keV. As mentioned in previous sections of this chapter, one of the parameters of interest to microscopists, and which is primarily relevant for imaging is the MTF.

Figure 7.14 demonstrate the MTF of this direct CCD (*pn*CCD) detector in comparison to a conventional indirect CCD-based electron detector. Clearly, direct detection is superior to conventional indirect detection, because it is still able to record and display high spatial frequency information where the conventional camera fails to do this. This dramatic improvement however, is a direct proof that a reduced number of optical interfaces (no fiber-optics, no scintillator) and thus a reduced number of sites that may cause scattering and signal spreading holds great potential for significant detector improvement.

However, this MTF is the result of ultra-low-dose experiments using electrons. The TEM was adjusted in such manner that the electron dose, incident on the

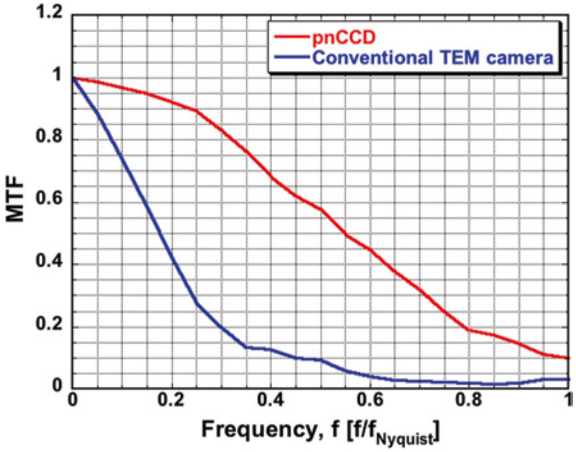

Fig. 7.14 MTF comparing a conventional CCD-based electron detector (indirect detection) to a novel direct electron detector

direct CCD detector, was set to the lowest possible setting. Images were recorded with exposure times of 100 s. A major drawback of such very long exposure times is a compromised spatial resolution in the image due to sample drift (certainly noticeable at high magnifications). Nevertheless, MTF measurements using the knife-edge method could be performed without being negatively affected by sample drift. Furthermore, this ultra-low-dose setting allowed the center of gravity algorithm to be fully exploitable. As mentioned previously, this algorithm relies on electron scattering simulations inside the pixel and the energy deposited by the electron into the pixel. Equipped with such an algorithm the spatial resolution is increased to 5 μm allowing a more accurate positioning of the electron entrance location in detector-space. In practice this single-electron read-out mode enables single electron detection as long as the incident dose corresponds to single-electron illumination conditions.

However, in real electron imaging more than just one electron at a time is registered by each pixel. Detector read-out speed controls the amount of electrons (per pixel per unit time) that can be processed as single-electron events. If the incident dose of electrons exceeds the processing speed, i.e., two or more electrons are registered within one pixel during one read-out cycle, then the back-tracking and positioning algorithms will be infinitely more difficult to handle. Naturally, any large number of electrons that one encounters during 'regular' TEM use will render this back-tracking approach highly impractical.

A small number of prototype detectors are designed to then default to signal integration mode, departing from single-electron counting mode permitting to maintain their operational readiness and expanding their application flexibility.

In conclusion, direct detection systems promise to outperform conventional electron imaging detectors. Some characteristic parameters, which are relevant for imaging, demonstrate this already on a number of prototypes, and there still is room for improvement and fine-tuning of detector fabrication and performance parameters.

7.2 Detectors for X-rays

7.2.1 Introduction

X-ray sources have traditionally been used for the investigation of static structures, rather than dynamic processes using time-resolved or in-situ experiments. There are various reasons for this, and a few of these are listed here without an attempt for completeness. One very important reason is the limited flux at the sample produced by laboratory based X-ray sources, which results in relatively long exposure times. Therefore, only relatively slow processes can be studied. This is particularly true for scattering based experiments, where a significant part of reciprocal space needs to be sampled in order to be able to perform reliable Fourier transforms to real space. The situation is more favorable for direct X-ray imaging experiments, but in this case the spatial resolution is limited to a few tens of micrometers at best. Another limitation for some in-situ and time-resolved experiments is the use of complicated sample environments, like furnaces, or reaction cells, which requires high energy X-rays with sufficient penetration power. The increase in X-ray energy means a dramatic decrease in the scattering power of the sample, increasing the required exposure times.

The available photon flux at the sample has increased exponentially over the last decades; with the improvement of storage ring based synchrotron sources (see following section). However, time-resolved and in-situ experiments generally require dedicated and often complicated sample environments, which are difficult to develop for an external user of a user-facility where access to measurement time is severely limited. Real progress and groundbreaking results have been obtained at synchrotrons in the cases where an experimental station is fully dedicated to specific time-resolved or in-situ experiments. One example is the time-resolved beamline ID09 at the European Synchrotron Radiation Facility in Grenoble, France. With the increase of the number of synchrotron storage rings and experimental stations worldwide this situation is expected to improve in the future.

Another reason for the relatively low number of time-resolved and in-situ experiments as compared to the number of static and ex-situ experiments is the lack of suitable X-ray detectors. Traditionally, the development of X-ray detectors has been lacking behind the development of the storage ring X-ray sources. This is not so much because of a lack of detector developments, but rather because of the exponential increase in source brilliance. Furthermore, every facility has only one source, but many tens of different X-ray detectors. A number of detector systems have been developed specifically for time-resolved and in-situ experiments and some of these will be discussed in this chapter.

Fig. 7.15 Source brilliance as function of time

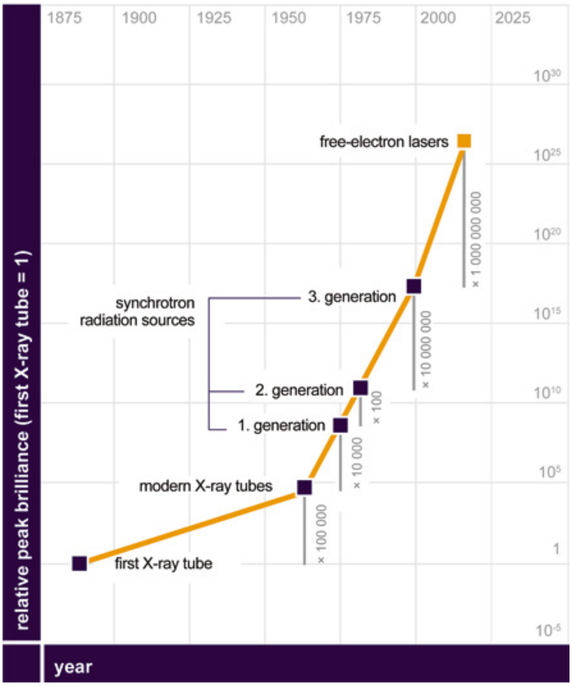

7.2.2 *Storage Ring Based X-ray Sources*

7.2.2.1 Source Developments

X-ray storage ring sources have developed spectacularly over the last 30 years, thanks to progress in storage ring accelerator technologies. This is best illustrated by the source brilliance as function of time given in Fig. 7.15, which shows an increase by one order of magnitude every 3 years.

Brilliance is not equivalent to flux, since it includes the sources size as well as the beam divergence, which both have decreased dramatically over time. However, it is the most relevant parameter in many experiments, since a high brilliance beam allows focusing many photons onto a small spot. This is important since either the samples themselves are small (micrometers to millimeters), or only a small volume of the sample is to be investigated. It is difficult, if not impossible, to translate the evolution of the source brilliance into an evolution of the number of photons in the detector, or detector volume. But even though a significant part of the increase in source brilliance has been offset by a parallel decrease in sample size and an evolution towards weaker scattering events, it is unambiguous that there has been a correlated increase in the flux on the detector. This increased measured intensity has made possible a corresponding decrease in exposure times, which opened the way for many time-resolved and in-situ X-ray experiments. Another important development, besides this exponential increase in source brilliance, is the increase in number of sources, and thus available experimental stations worldwide.

What follows in the Sect. 7.2.2.2 are some illustrative examples of 2-dimensional X-ray detectors used in in-situ and time-resolved experiments at synchrotron sources. A distinction has to be made between so-called "integrating" and "photon counting" detectors. Integrating detectors, integrate the total signal, produced by the X-rays as well as by the noise, during a user determined integration time. Since there is no signal processing during the integration period large fluxes can be recorded. This is not to be confused with read-out speed. For example, the read-out speed of CCDs is relatively low, whereas they can record large instantaneous fluxes. The down side is that the noise is also integrated. In photon counting detectors, the signal generated is amplified and compared to a threshold, providing a means to discriminate between noise and photons, and thus providing near noise free detectors. The down side in this case is the time it takes to amplify and process the signal, thus limiting the number of counts per second that can be recorded.

7.2.2.2 Examples of Detectors for In-situ Experiments at Storage Rings

In this chapter we will give three examples where the X-ray detector has played an essential role in enabling in-situ or time-resolved experiments. It is impossible, and by no means attempted, to be complete or to give a balanced representation, and many examples that could be included are omitted. We will concentrate on X-ray scattering experiments, but would like to stress that both imaging and spectroscopy techniques have very successfully been used in time-resolved and in-situ experiments. Furthermore, we will limit ourselves to 2-dimensional solid-state detectors.

The Cornell AP-HPAD

One of the first hybrid pixel detector systems specifically developed for fast in-situ and time-resolved experiments at synchrotron sources is the Analogue Pipeline Hybrid Pixel Array Detector (AP-HPAD), developed by the group of Sol Gruner at CHESS/Cornell [38–40]. The system was designed for fast time-resolved imaging experiments, with micro-second framing times. In order to get statistically meaningful data within micro-seconds, photon counting is not an option and an integrating detection scheme is mandatory. To optimize the efficiency of the experiments 8 consecutive images can be recorded and stored within the pixel, before reading out the detector. The schematic pixel layout of the system is shown in Fig. 7.16, and has been the basis for other systems including the Adaptive Gain Integrating Pixel Detector (AGIPD) detailed below.

Early small-scale prototypes of this system have been successfully used for high-speed radiography experiments of fuel injectors [41, 42]. In these experiments a high-pressure common-rail diesel injection system typical of that of

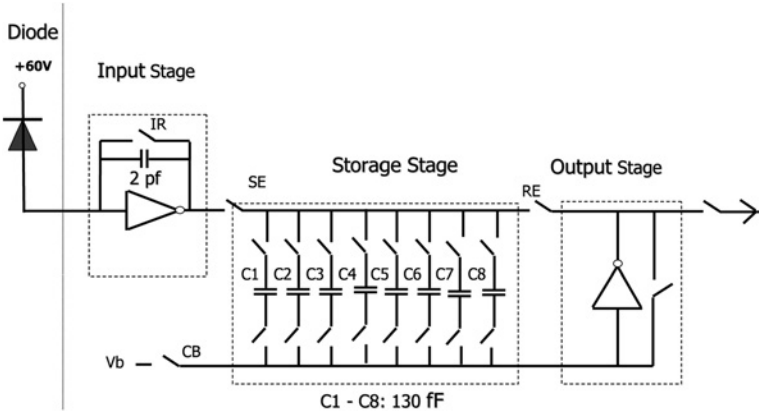

Fig. 7.16 Pixel layout of the Cornell analogue pipeline HPAD chip, [40]

a passenger car was used to study the ultra-sonic and shock wave behavior of the diesel fuel vapor immediately after exiting the orifice. The details of the three-dimensional density distribution as well as the transient behavior turned out to be considerably more complex then originally expected. The microsecond time resolution of the detector as well as the perfect repeatability and triggerability of the system under study were essential for this experiment.

The PILATUS detector

The PILATUS detector was developed by the Paul Scherer Institute for protein crystallography at the Swiss Light Source [43]. In contrast to the above described AP-HPAD, it is a photon counting detector, which has the advantage of near zero noise and excellent stability in time, as explained in the introduction. The drawback is that photon counting automatically limits the instantaneous flux that can be recorded. With a maximum count rate per pixel of the order of 10^6 counts per second, exposure times of a microsecond, used in the previous example, will yield statistically meaningless intensities. However, the system is well suited for both time-resolved and in-situ experiments. The PILATUS can be gated fast enough to isolate a single bunch of for instance the Advanced Photon Source operating in 24 bunch mode, with 153 ns separation between consecutive bunches [44]. This results in a time resolution determined by the X-ray pulse length. Similar time resolutions have been obtained before by isolating single pulses using a series of fast mechanical shutters, including fast spinning disks with slotted holes [45], which is only possible on a dedicated experimental station. The gated PILATUS detector can then be used in pump-probe experiments, where a pump, usually an optical laser, excites the sample, and a given time delay later the X-ray pulse measures the state of sample. This is then repeated many times, until enough statistics has been

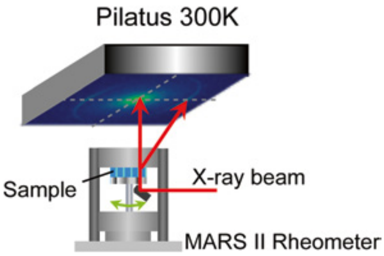

Fig. 7.17 Experimental setup in-situ rheometer with PILATUS 300K pixel detector

accumulated, after which the delay between pump and probe is changed, and the measurement repeated. The possibilities have been demonstrated in an experiment performed on polycrystalline organic thin films of α-perylene [44].

The PILATUS detectors have been used in a large number of in-situ experiments, including surface diffraction, powder diffraction and small angle scattering. We present here a recent experiment where small angle X-ray scattering is combined with in-situ rheology [46]. Small angle scattering gives access to nanoscopic length scales, and is well suited for millisecond and slower processes. Rheology probes the viscoelastic properties of fluid materials under steady or oscillatory shear conditions. Struth et al. used a vertical scattering geometry in order to have access to otherwise inaccessible sample orientations. The unique setup including a specially designed X-ray optical element and a modified HAAKE MARS II rheometer gives enough freedom to vary the sample-to-detector distance to the desired value (see Fig. 7.17). A PILATUS 300K system was used to record two-dimensional scattering patterns. The unique combination of in-situ rheology and a fast area detector resulted in the observation of new states of liquid crystal 8CB under nonlinear shear conditions [46]. Due to the noise free characteristics of the Pilatus module, even the weakest signals from the sample could be detected in reasonable time scales. Since beam damage is always an issue for soft condensed matter materials, fast detection times are crucial for such kind of experiments. On the other hand the time resolution in this experiment was not limited by the speed of the detector but by the flux of the source.

7.2.3 Free-Electron Laser Based X-ray Sources

7.2.3.1 Source Developments

As shown in Sect. 7.1.2.1, and Fig. 7.15, storage ring based synchrotron X-ray sources have seen an exponential increase in brilliance, revolutionizing X-ray science as well as X-ray detectors. However, this trend will not continue with storage ring based sources, as the newest sources are already very close to what is considered as the "ultimate storage ring". The next generation of sources are Free-Electron Lasers (FEL), using linear accelerators instead of circular storage rings. A thorough discussion of source and accelerator physics is far beyond the scope of

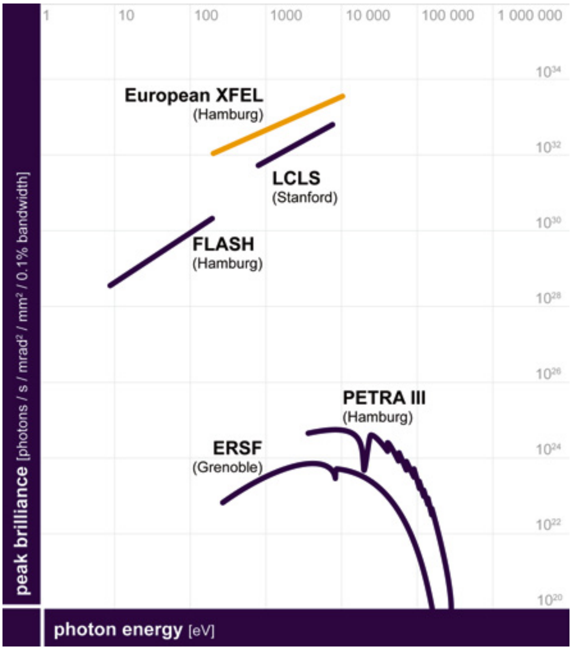

Fig. 7.18 Peak brilliance of FEL sources as compared to storage ring sources

this chapter, but it is important to discuss some of the principles involved, as they have crucial consequences for the beam characteristics and thus also for the X-ray detectors involved.

The FEL sources are based on the Self-Amplified Spontaneous Emission (SASE) principle, where the electrons inside a single bunch interact with their own radiation field while traversing the insertion devices. As a result the electrons start emitting radiation in phase, with the result that the total intensity becomes proportional to the square of the number of electrons in a bunch. This is to be compared to storage ring sources where the electrons emit incoherently, and thus the intensity is only proportional to the number of electrons in the bunch. A number of conditions have to be fulfilled in order for the electrons to interact with their own radiation field, and emit coherently. Firstly, the electron bunches have to be very compact, in order to have a sufficiently large electron density. This is hard to achieve in storage rings, which are equilibrium sources. In single-pass linear accelerators there is no need for equilibrium, and the electron bunch can be highly compressed. As a result, not only is the generated X-ray pulse very intense, it is also very short, typically in the femtosecond range, which is to be compared to tens of picoseconds for storage rings. In summary, the photon pulse length is more than a 1000 times shorter than at classical 3rd generation synchrotron storage rings, the horizontal emittance is by a factor of 100 smaller, and the vertical emittance by a factor of 3, while the number of photons per pulse is more than a factor of 300 higher, and the natural monochromaticity a factor of 10 better, giving an increase in peak brilliance by more than 9 orders of magnitude (Fig. 7.18). Another major difference is the fact that the FEL beams are fully laterally coherent. It is evident that these improvements will allow for new science to be performed with the consequence that new types of X-ray detectors are required [47].

7.2.3.2 Requirements for X-ray Detectors for FEL Based Sources

A detailed description of the specifications for the X-ray detectors for Free Electron Laser sources based on scientific requirements can be found in [47]. However, it is important to point out that the field of X-ray FEL science is still in its infancy and developing rapidly, meaning that scientific requirements and detector specifications will evolve over the coming years. Nevertheless, a few specifications, resulting from the high intensity per pulse, can safely be given, and will be discussed here.

The high intensity per pulse will not only allow for, but often impose single-shot experiments. Due to the high flux of the refocused beam, samples will often not survive a single pulse because of ionization and subsequent coulomb-explosion [48]. However, since the pulse is very short, the sample will provide a full diffraction pattern before sample disintegration sets in, the so-called diffract-before-destroy principle [49, 50]. As a consequence X-ray detectors will have to record a complete diffraction image for every X-ray pulse. This means that, first of all, the X-ray detectors will have to cover a sufficiently large part of reciprocal space, with sufficiently fine pixellation. Both the size of the detector and the number of pixels required depend on the targeted scientific application [47], but generally a few million pixels of few hundred microns are required. Since a full diffraction pattern, spanning a large dynamic range, needs to be recorded per pulse (<100 fs) photon counting is excluded, leaving integrating detectors as the only option. In many experiments it is essential to distinguish between 0 and 1 photon, meaning that the detector needs to be low noise, which is particularly challenging for integrating detectors. At the same time the most intense pixels need to be able to handle more than 10^4 photons per pulse. For single-shot experiments with randomly oriented samples it is not known a priori which pixels will see low and which high intensity. Finally, the intense beam will generally prohibit the use of beam stops in front of the detector, as is customary in storage ring source experiments, and consequently the detector will need to have a central hole for the direct beam to pass through.

The requirements given above are valid for all X-ray Free-Electron Lasers, independent of the exact time structure. The European XFEL, with its super-conducting accelerator technology, presents an additional challenge, as compared other projects using so-called warm technology (LCLS in the USA and SCSS in Japan). In Fig. 7.19 the time structure of the European XFEL is shown. Bunch trains, with up to 2700 bunches separated by 220 ns are repeated 10 times per second. Since a mega-pixel detector cannot be read out in 220 ns, images will have to be stored inside the pixel for readout during the 99 ms inter-train periods. This significantly complicates the pixel design, as well as it limits the minimum pixel size obtainable.

Fig. 7.19 Time structure of the European X-ray free electron laser in Hamburg

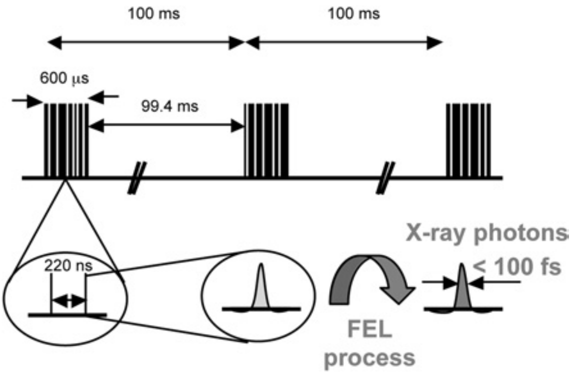

There are a number of detector development projects for X-ray FELs worldwide and a detailed technical description of these can be found in [51 and references therein]. The system most used to date, however, is the pnCCD adapted from astronomy applications [37] and as discussed also in the Sect. 7.2.3.1 on electron detectors—novel direct electron detectors.

For the European XFEL there are three projects ongoing, each one attempting to achieve the large dynamic range and the in-pixel frame storage in different technical ways. The Large-Pixel Detector (LPD) project uses three gains (high/medium/low) in parallel, and stores the images in an analogue pipeline [52]. The DEPFET Sensor with Signal Compression (DSSC) project uses a non-linear response of the sensor, and a digital memory for image storage [53]. The Adaptive Gain Integrating Pixel Detector (AGIPD) project uses an automatically adapted gain to cover the large dynamic range, and an analogue memory for image storage [54]. The AGIPD project will be presented in more detail in the Sect. 7.2.3.3.

7.2.3.3 The Adaptive Gain Integrating Pixel Detector Project

The AGIPD detector is a Hybrid Pixel detector with a silicon diode array bump-bonded to a pixellated readout chip (Application Specific Integrated Circuit, ASIC) and is being designed and built by a consortium consisting of DESY in Hamburg, the Swiss Light Source at the Paul Scherer Institute in Switzerland and the Universities of Hamburg and Bonn (Germany). Dynamic gain switching is used to provide the required large dynamic range. In this concept each pixel automatically adjusts the gain of its pre-amplifier according to the incoming signal strength, without any external intervention, and for every X-ray pulse in the bunch train. There are three possible gain settings: high, medium and low, which together cover a dynamic range from single photon sensitivity to 10^4 photons of 12 keV. As stated above, the X-ray pulses in the bunch train are separated by 220 ns (4.5 MHz), which is too short to read out the entire detector. Images are therefore stored in an analogue memory, which is randomly accessible. This last feature is important, since at most

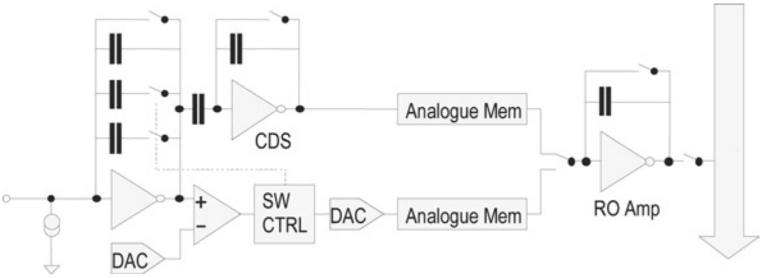

Fig. 7.20 Schematic layout of the AGIPD pixel cell

350 images can be stored, which is significantly less than the possible maximum of 2700 images available from the European XFEL source. The detector is therefore laid out for vetoing and image overwriting, such that only good images are stored. The analogue memory is then read out and digitized during the 99.4 ms train intervals. A schematic layout of the pixel cell is given in Fig. 7.20.

Detailed measurements on various prototypes are still under way, but the essential gain switching as well as the random access analogue memory have been proven to work. The current pixel size of 200 μm is a compromise between the scientific push for small pixels and the technological limitations to integrate enough functionality and storage capacity in the pixel. A single readout ASIC, the fundamental building block, will have 64 × 64 pixels. The ultimate 1k × 1k pixel detector will be constructed using monolithic multi-chip modules, with 2 × 8 readout chips (128 × 512 pixels), as indicated in Fig. 7.21, and is foreseen to be ready by 2014.

Although AGIPD, is specifically developed for the European XFEL, with its unique time structure (see Fig. 7.19), it also offers great opportunities for time-resolved and in-situ X-ray experiments at storage ring sources. Since it is an integrating detector, it does not suffer from count rate limitations, which often limits the time resolution when using photon counting detectors. At the same time, up to 350 images can be recorded in very fast succession, down to 220 ns or 4.5 MHz. This could be used in, for instance, pump-probe experiments, where a trigger initiates a reversible or repeatable reaction and the evolution of sample is then followed in 220 ns intervals. This can then be repeated 10 times per second. Since the operation of the detector is fully triggered by external signals, there is a considerable freedom in the sampling rate. For instance one could follow the sample shortly after the pump has initiated a change at 220 ns time intervals, and gradually increase this spacing. There are, however, some technological limits to the degrees of freedom. Since an analogue memory is used to store the signal inside each pixel, one has to read out the images within a given time, otherwise the stored signal will slowly fade away due to the so called signal droop. The full extend of the limitations of the degrees of freedom will only become clear once the final readout ASIC is ready and fully tested.

It should be pointed out that, although developing a system like AGIPD is a multi year and multi million Euro project, deriving variations, optimized for storage ring applications, is considerably faster and cheaper.

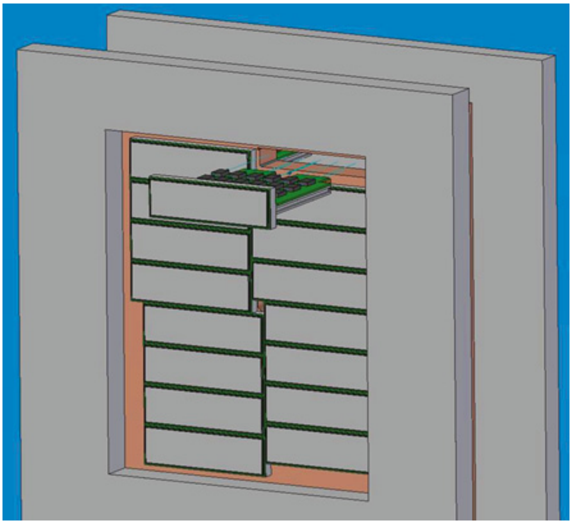

Fig. 7.21 Layout of the final 1k × 1k detector, featuring a central hole for the primary beam

7.2.4 Outlook

X-ray detectors have traditionally been the weakest part in many synchrotron-based experiments, especially in time-resolved and in-situ experiments. This is not due to a lack of progress in detector technology, but rather due to the phenomenal increase in source brilliance over the last decades. Since this brilliance increase is leveling of for storage ring based X-ray sources, an increased emphasis is put on detector development. Although it is impossible to give an accurate prediction of the future, a few directions and expected developments should be mentioned.

For synchrotron experiments there is a clear shift away from using or adapting detectors or components developed for other scientific or non-scientific applications, towards custom made detector systems. A good example is the PILATUS based system developed specifically for protein crystallography experiments [43]. This trend is continuing with, for example, the AGIPD development mentioned above. The hybrid pixel array detector technology with Application Specific Integrated Circuits (ASICs), will show a trend towards using more intelligence inside the pixel, like the automatically adapting gain or communicating pixels [55, 56]. Using new developments in industry, like the 3-dimensional integration of CMOS technology [57] one can dramatically increase the functionally per unit area, or alternatively decrease the pixel size, while keeping full functionally. This 3D-integration will also open the way for building 4-side buttable detector modules, which can be tiled together into large detector systems, with negligible dead areas. In parallel to the developments in the readout electronics, we are seeing rapid developments in the sensor technology, like 3D and edgeless silicon [58] or high-Z semiconductors [59] for high photon energies. With avalanche diode arrays or silicon PMTs one will be able to reach time resolutions down to the nano-second level [60], while low noise, and thus high-energy resolution can be obtained with DEPFET based pixel sensors [53]. In the coming years we will see various combinations of the above possibilities. It might not be impossible that we will be able to determine for every recorded photon its energy with near Fano limited resolution, and assign it to the electron bunch that generated it, thus reaching machine limited energy, as well as time-resolution in the long term.

References

1. C. Ponchut, J. Synchrotron Radiat. **13**, 195 (2006)
2. J.D. Dainty, R. Shaw, *Image Science* (Academic Press, London, 1974)
3. K.H. Herrmann, D. Krahl, *Advances in Optical and Electron Microscopy*, vol. 9 (Academic Press, London, 1984), p. 1
4. K. Ishizuka, Ultramicroscopy **52**, 7 (1993)
5. J.M. Zuo, Ultramicroscopy **66**, 21 (1996)
6. A.L. Weickenmeier, W. Nüchter, J. Mayer, Optik **99**, 147 (1995)
7. O.L. Krivanek, P.E. Mooney, Ultramicroscopy **49**, 95 (1993)
8. W.J. de Ruijter, J.K. Weiss, Rev. Sci. Instrum. **63**, 4314 (1992)
9. K. Downing, D.A. Grano, Ultramicroscopy **7**, 381 (1982)
10. P.J.W. Noble, IEEE Trans. Electr. Dev. **ED15**, 202 (1968)
11. S.G. Chamberlain, IEEE J. Sol. Stat. Circ. **SC4**, 333 (1969)
12. P.K. Weimer, W.S. Pike, G. Sadasiv, F.V. Shallcross, L. Meray-Horvath, IEEE Spectr. **6**, 52 (1969)
13. E.R. Fossum, Proc. SPIE **1900**, 2 (1993)
14. B. Dierickx, G. Meyants, D. Scheffer, in *Proceedings of IEEE CCD & AIS Workshop* (1997), p. P1
15. G. Deptuch, Nucl. Instrum. Meth. Phys. Res. A, **543**, 537 (2005)
16. G. Mettivier, Nucl. Instrum. Meth. Phys. Res. A, **516**, 554 (2004)
17. S.R. Amendolia, et al., Nucl. Instrum. Meth. Phys. Res. A, **466**, 74 (2001)
18. R.H. Richter et al., Nucl. Instrum. Meth. Phys. Res. A, **511**, 250 (2003)
19. M. Battaglia et al., Nucl. Instrum Meth. Phys. Res. A, **608**, 363 (2009)
20. G. McMullan et al., Ultramicroscopy **107**, 401 (2007)
21. P. Bartl et al., Nucl. Instrum. Meth. Phys. Res. A, **591**, 314 (2007)
22. R. Turchetta et al., Nucl. Instrum. Meth. Phys. Res. A, **458**, 677 (2001)
23. J. Matheson et al., Nucl. Instrum. Meth. Phys. Res. A, **608**, 199 (2009)
24. A. Blue et al., Nucl. Inst. Meth. Phys. Res. A, **581**, 287 (2007)
25. H.S. Matis et al., IEEE Trans. Nucl. Sci. **50**, 1020 (2003)
26. N.H. Xuong et al., Proc. SPIE-IS&T Elect. Imag. **5301**, 242 (2004)
27. G. Varner et al., Nucl. Instrum. Meth. Phys. Res. A, **541**, 166 (2005)
28. G. McMullan, S. Chen, R. Henderson, A.R. Faruqi, Ultramicroscopy **109**, 1126 (2009)
29. M. Deveaux et al., Nucl. Inst. Meth. Phys. Res. A, **583**, 134 (2007)
30. J. Bogaerts, B. Diericks, G. Meynants, D. Uwaerts, IEEE Trans. Electr. Dev. **50**, 1 (2003)
31. M. Deveaux et al., Nucl. Inst. Meth. Phys. Res. A, **552**, 118 (2005)
32. E.G. Villani, R. Turchetta, M. Tyndel, Nucl. Phys. B **125**, 184 (2003)
33. L. Strüder et al., Astron. Astrophys. **365**, L18 (2001)
34. W. Leitenberger et al., J. Synchrotron Radiat. **15**, 449 (2008)
35. R. Hartmann et al., Nucl. Instrum. Meth. Phys. Res. A, **568**, 188 (2006)
36. N. Meidinger et al., IEEE Trans. Nucl. Sci. **45**, 2849 (1998)
37. L. Strüder et al., Nucl. Instrum. Meth. Phys. Res. A, **614**(3), 483 (2010)
38. S.L. Barna et al., IEEE Trans. Nucl. Sci. **44**, 950 (1997)

39. E.F. Eikenberry et al., J. Synchrotron Radiat. **5**, 252 (1998)
40. G. Rossi et al., J. Synchrotron Radiat. **6**, 1096 (1999)
41. A.G. MacPhee et al., Science **295**, 1261 (2002)
42. W. Cai et al., Appl. Phys. Lett. **83**, 1671 (2003)
43. P. Kraft et al., IEEE Trans. Nucl. Sci. **56**, 758 (2009)
44. T. Ejdru et al., J. Synchrotron Radiat. **16**, 387 (2009)
45. M. Wulff et al., Faraday Discuss. **122**, 13 (2002)
46. B. Struth et al., Langmuir **27**, 2880 (2011)
47. H. Graafsma, JINST **4**, P12011 (2009)
48. R. Neutze, R. Wouts, D. van der Spoel, E. Weckert, J. Hajdu, Nature **406**, 752 (2000)
49. H. Chapman et al., Nature **470**, 73–77 (2011)
50. M.M. Seibert et al., Nature **470**, 78–81 (2011)
51. H. Graafsma, *Semiconductor Radiation Detection Systems* (CRC-Press, Boca Raton, 2010), ISBN: 9781439803851
52. A. Blue, M. French, P. Seller, V. O'Shea, Nucl. Instrum. Meth. Phys. Res. A, ***607***, 55–56 (2009)
53. M. Porro et al., in *IEEE Nuclear Science Symposium Conference Record* (2008), p. 1578
54. X. Shi et al., Nucl. Instrum. Meth. Phys. Res. A, **624**, 387 (2010)
55. R. Ballabriga, M. Campbell, E. Heijne, X. Llopart, L. Tlustos, IEEE Trans. Nucl. Sci. **NS-54**, 1824 (2007)
56. D. Pennicard, R. Ballabriga, X. Llopart, M. Campbell, H. Graafsma, Nucl. Instrum. Meth. Phys. Res. A, **636**, 74 (2011)
57. International Technology Roadmap for Semiconductors (ITRS) report 2009, and 2010 update interconnection section; www.itrs.net
58. S.I. Parker, C.J. Kenney, J. Segal, Nucl. Instrum. Meth. Phys. Res. A, **395**, 329 (1997)
59. D. Greiffenberg, A. Fauler, A. Zwerger, M. Fiederle, JINST **6**, C01058 (2011)
60. C. Thil et al., Nucl. Instrum. Meth. Phys. Res. A, **628**, 461 (2011)